Authors' accepted manuscript
Article published in *International Journal of Engine Research*, February 19, 2021
The final publication is available at https://doi.org/10.1177%2F1468087421993961

Eulerian–Lagrangian CFD-microphysics modeling of a near-field contrail from a realistic turbofan

S. Cantin*, M. Chouak, F. Morency, and F. Garnier

École de technologie supérieure, 1100 Notre Dame Street West, University of Quebec, Montreal H3C1K3, Canada

Abstract

Aircraft contrails contribute to climate change through global radiative forcing. As part of the general effort aimed at developing reliable decision-making tools, this paper demonstrates the feasibility of implementing a Lagrangian ice microphysical module in a commercial CFD code to characterize the early development of near-field contrails. While engine jets are highly parameterized in most existing models in a way that neglects the nozzle exit-related aspects, our model accounts for the geometric complexity of modern turbofan exhausts. The modeling strategy is based on three-dimensional URANS simulations of an aircraft nozzle exit involving a bypass and a core jet (Eulerian gas phase). Solid soot and ice particles (dispersed phase) are individually tracked using a Lagrangian approach. The implemented microphysical module accounts for the main process of water-vapor condensation on pre-activated soot particles known as heterogeneous condensation. The predictive capabilities of the proposed model are demonstrated through a comprehensive validation set based on the jet-flow dynamics and turbulence statistics in the case of compressible, turbulent coaxial jets. Simulations of contrail formation from a realistic nozzle-exit geometry of the CFM56-3 engine (short-cowl nozzle delivering a dual stream jet with a bypass rate of 5.3) were also carried out in typical cruise flight conditions ensuring contrail formation. The model provides reliable predictions in terms of the plume dilution and ice-particle properties as compared to available in-flight and numerical data. Such a model can then be used to characterize the impact of nozzle-exit parameters on the optical and microphysical properties of near-field contrails.

Keywords: *contrails, CFD, microphysics, coupling, aircraft engine, Eulerian–Lagrangian approach, ice particle growth.*

1. NOMENCLATURE

A	=	Kelvin effect
C_ρ	=	factor for control water-vapor temperature above the particle surface
C_T	=	factor for control water-vapor density above the particle surface
D_b, D_c	=	bypass, core diameter, m
D_{cont}	=	contrail diameter, m
D_p	=	inner primary jet diameter, m
D_s	=	inner secondary jet diameter, m
ε	=	dissipation rate, $m^2.s^{-3}$

* Corresponding author: sebastien.cantin.1@ens.etsmtl.ca

$\varepsilon_{\text{coarse}}^{12}$	=	mean relative error between coarse and medium meshes
$\varepsilon_{\text{fine}}^{23}$	=	mean relative error between medium and fine meshes
$\text{GCI}_{\text{coarse}}^{12}$	=	GCI index between coarse and medium meshes
$\text{GCI}_{\text{fine}}^{23}$	=	GCI index between medium and fine meshes
k	=	turbulent kinetic energy, $m^2.s\text{-}^2$
L	=	computational domain length, m
L_{noz}	=	nozzle length, m
λ_w	=	wavelength, m
M_b, M_c	=	core, bypass Mach number
$\dot{m}_{fuel}$	=	specific fuel consumption, $kg.s^{-1}$
m_p	=	mass particle, kg
μ_r	=	refractive index
N	=	dilution ratio
$N_{com,g}$	=	number of particles computed in a grid cell
N_g	=	total number of particles in a grid cell
N_{com}	=	number of particles computed
N_D	=	dilution ratio based of the contrail diameter, D_{cont}
N_{exit}	=	number of particles at core-engine inlet, m^{-3}
N_p	=	number of physical particles per computed particle
N_Z	=	dilution ratio based on the passive scalar Z
n	=	particle-number density, m^{-3}
P_{amb}, P_{amb}^0	=	far-field, free-stream ambient pressure, Pa
$P_b,\ P_c$	=	bypass, core-pressure inlet, Pa
$\overline{p}_g$	=	mean gas pressure, Pa
P_{tot}	=	total pressure, Pa
P_w	=	vapor partial pressure, Pa
$P_{w,liq}^0$	=	saturation vapor pressure above liquid water, Pa
Q_{ext}	=	Mie extinction efficiency
$\overline{\rho}_g$	=	mean gas density, $kg.m^{-3}$
ρ_p	=	particle density, $kg.m^{-3}$
R	=	computational domain radius, m

$r_p, r_{p,0}$	=	particle radius, initial particle radius, m
r_g	=	specific gas constant, J.mol^{-1}.K^{-1}
$\sigma_{\text{coarse}}^{12}$	=	standard deviation between coarse and medium meshes
$\sigma_{\text{fine}}^{23}$	=	standard deviation between medium and fine meshes
S	=	saturation ratio
t	=	time, s
τ	=	optical depth
T_{amb}, T_{amb}^0	=	far-field, free-stream ambient temperature, K
$T_b, T_c,$	=	bypass, core temperature inlet, K
$\overline{T}_g$	=	mean gas temperature, K
$\tilde{T}_p$	=	mean particle temperature, K
U_b, U_c	=	bypass, core velocity, m.s^{-1}
U_{cruise}	=	initial aircraft speed, m.s^{-1}
$\tilde{\boldsymbol{u}}_g$	=	mean gas velocity, m.s^{-1}
$\tilde{\boldsymbol{u}}_p$	=	mean particle velocity, m.s^{-1}
U_p, U_s	=	primary-, secondary-jet velocity, m.s^{-1}
V	=	aircraft speed, m.s^{-1}
$\overline{\omega}_{\text{ice}}$	=	coupling term for mass transfer rate, kg.m^{-2}.s^{-1}
X_{amb}	=	ambient mole fraction of water vapor
X_c	=	core flow mole fraction of water vapor
X_w	=	mole fraction of water vapor
$\boldsymbol{x}_p$	=	particle position
$\tilde{Y}_a$	=	mean mass fraction of air
$\tilde{Y}_w$	=	mean mass fraction of water vapor
Z	=	passive scalar

2. INTRODUCTION

The continuous growth in air passengers by about 5% per year has increased scientific concerns about the climate impact of commercial aviation.[1] Cruise flights contribute to global warming through soot and water-vapor emissions from aircraft engines that are responsible for visible white condensation trails (contrails) behind aircraft.[2, 3] Persistent contrails composed mainly of supersaturated ice crystals survive in the atmosphere for several hours and even evolve to form large cirrus formations referred to as aircraft-induced clouds (AIC).[4] The spreading and persistence of this artificial cloudiness in the atmosphere determine their impact on the earth's radiative balance.[5] Global assessments[6] show that the impact of linear contrails is about 3–9·10^{-3} W.m^{-2}, while the impact of AIC is 10 times higher,[6] which

corresponds to 3 times the impact of aviation CO_2 alone.[7] For this reason, the contrail formation process has been a topic of increasing interest in the literature. Owing to both complexity and onerous costs of in-flight measurements, the development of innovative mitigation strategies has to be based on reliable decision-making tools. As such, several modeling approaches with different levels of microphysics/dynamics representations have been used in literature to investigate contrails. The following is a short review of main approaches and findings.

Modeling contrail life cycle involves several scales ranging from local scales in the engine jet phase (t ~ 0-10 s after the exhaust emission) to the global scale in the dispersion phase (few minutes to hours after the exhaust emission) (see Figure 1). From the thermodynamic point of view, the revised Schmidt–Appleman criterion[8] helps to determine atmospheric regions of contrail occurrence based on water liquid saturation conditions. This criterion was used to initiate contrail formation in global models, such as in the Contrail Cirrus Prediction Tool (CoCiP),[9] and made it possible to assess the global environmental impact of contrails. To allow coverage of the full evolution cycle of a large population of contrails, the physics modeling was relatively simplified, such as for initialization of the species concentration with a Gaussian profile. Even though the results of regional air-traffic simulations[9, 10] were quite consistent with in-flight measurements and satellite observations, the microphysical processes of ice production remain misunderstood. A more precise characterization of ice particles was achieved using 0-D microphysical trajectory box models.[11, 12] This class of models allows detailed chemical kinetics and microphysics in the engine jet phase. For instance, simulations of young contrails[11, 13] highlighted the domination of soot-induced heterogeneous freezing due to the large amount of emitted soot condensation nuclei from kerosene-fueled engines. In this respect, the reduction of soot emissions with the use of alternative jet fuels can help alter the optical properties of contrails.[14] The box model results for plume dilution, however, showed some discrepancies compared to in-flight measurements due to (1) the absence of a detailed turbulence modeling[11, 14] and (2) the simplified level of dynamics using averaged bulk exhaust (provided by semiempirical models).[11, 14] Some authors remedied the shortcomings through offline-coupling strategies with an external fluid-flow solver.[15, 16]

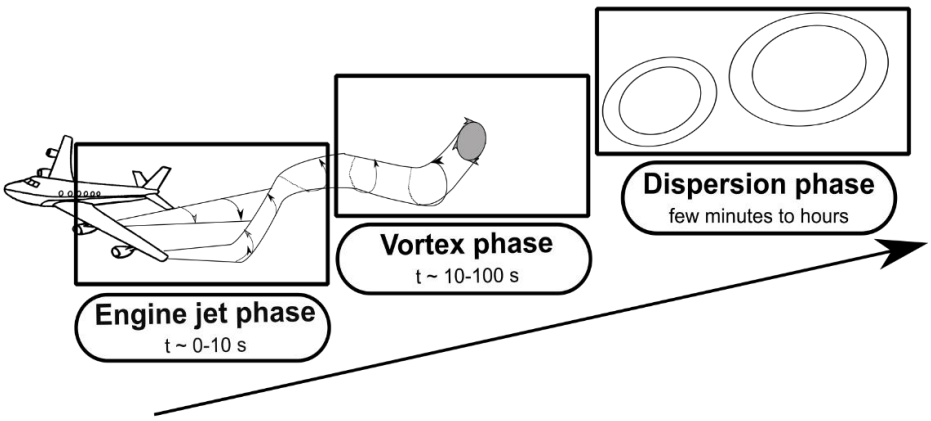

Figure 1: Evolution of a contrail in the wake of an aircraft

In the last two decades, computational cost-effectiveness has increased interest in 3D CFD-based models to refine the early plume dynamics and associated mixing process. Early plume properties are known to influence later contrail stages (optical depth, radiative forcing) as shown by the studies on the engine jet and vortex phase.[7, 17] As such, they are usually used as inputs in mesoscale models.[18, 19] Solid particles motion can be tracked in CFD using either an Eulerian[20] or a Lagrangian[21-23]. The former can capture the motion of higher particle concentrations[24] with either bulk parametrization[25, 26] or bins[20] for microphysics modeling. The simplest representation of particle-size distribution considers a single bin (monodisperse distribution) as used by Khou et al.[27, 28] who investigated the near-field contrails (engine jet phase) behind realistic commercial aircraft geometries using Reynolds-averaged Navier–Stokes (RANS) equations for turbulence modeling. Results revealed that wingtip vortices drained and cooled jets and highlighted the role of ambient relative humidity on ice-crystal properties. Using a single bin

could, however, prevent accurate estimates of ice-crystal concentration.[28] The most physically accurate treatment of ice particles in Eulerian terms considers size-resolved (binned) microphysics,[20] which avoids the problems of numerical diffusion inherent in bulk models[29, 30] that could lead to slight discrepancies in the dispersion of ice and water-vapor fields. The computational cost, however, is excessive (see the detailed review[31]).

In contrast, Lagrangian tracking allows for an explicit process-oriented modeling of ice microphysics,[30] which accounts for its popularity in contrail research for a while.[15, 22, 30] Most if not all Lagrangian studies are highly parameterized in a way that neglects nozzle exit-related aspects. For example, Paoli, Nybelen [32] modeled free turbulent jets with classical expansion laws to investigate contrail formation for two- and four-engine configurations. Unterstrasser and Görsch [33] also used Gaussian-like plume profiles to study the vortex phase and to characterize the impact of aircraft type on contrail evolution. These simplified representations of the nozzle exhaust jet do not allow for accurately taking into consideration the features of modern turbofan nozzles. As the flow structure and mixing in the early plume depend on engine exhaust parameters, the impact of high bypass rates and complex geometries (e.g., short and long cowls and chevrons) on the near-field microphysics remain unclear. This particularly motivated the development of a CFD-microphysical model that integrates the nozzle-exit geometry and avoids using parameterizations to describe the exhaust plume.

Therefore, the main objective of this study was to implement a Lagrangian microphysical module in a CFD code to simulate ice-particle growth in near-field contrails starting from a realistic turbofan nozzle exit. To the authors' knowledge, no contrail study has integrated the actual nozzle-exit geometry in a Lagrangian approach. A high-resolution spatial unsteady RANS method was therefore used to demonstrate the feasibility of the present approach. The paper is organized as follows. Section 2 begins with a description of the modeling approach, followed by the mathematical equations of fluid dynamics, particle motion, and ice microphysics. Section 3 describes the model and presents how the microphysical module was coupled to Simcenter Star-CCM+ CFD software. Section 4 discusses the validation test results for jet dynamics, plume dilution, and ice-particle properties.

3. MODEL DESCRIPTION

3.1 Approach for modeling the formation of near-field contrails

Figure 2 shows that the nozzle exit flow from a turbofan engine at cruise flight consists of two jets: a *hot* core flow and a surrounding *cold* bypass flow. Both jets are mixed with the freestream moist air. The bypass flow simply contains ambient moist air that has been slightly accelerated by the engine fan, while the core jet drives the fuel-combustion products composed of gaseous emissions laden with soot particles (dispersed or solid phase). Water vapor in the dilution plume condenses onto soot particles, which serve as condensation nuclei when activated with sulfuric acid (heterogeneous nucleation[11]). Under saturation conditions, ice particles form and grow by taking up more condensable matter—i.e., water vapor—from the plume and ambient air, leading to contrail formation.

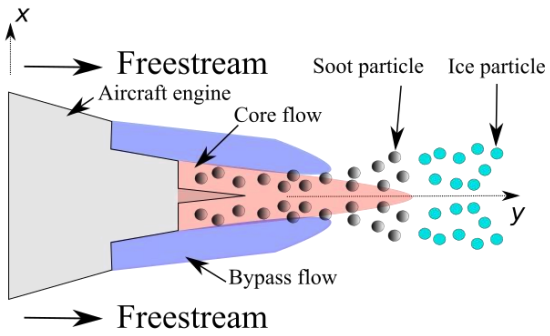

Figure 2: 2D scheme of exhaust flow from a turbofan engine with ice-particle formation

In this study, the Eulerian-Lagrangian approach was used to model the formation of contrail ice particles in the near field of an aircraft engine. The continuous gas phase was modeled with the Eulerian approach, while the dispersed-phase of solid particles (soot and ice particles) were tracked with the Lagrangian approach. Lastly, a one-way microphysical coupling was considered to account for ice-particle growth due to water-vapor condensation.

3.2 Gas-phase equations

The compressible flow of the gas phase ('g' index) is considered to be a mixture of two miscible species: air ('a' index) and water vapor ('w' index). Assuming an ideal gas, the mixture density $\overline{\rho}_g$, temperature $\tilde{T}_g$, and pressure $\overline{p}_g$ are linked with the equation of state:

$$\overline{p}_g = \overline{\rho}_g r_g \tilde{T}_g \tag{1}$$

where r_g is the specific gas constant. The overbar sign $-$ denotes the Reynolds (ensemble) averaging, while $\sim$ refers to the Favre (density-weighted) averaging defined as $\bar{\rho}\widetilde{\Phi} = \overline{\rho\Phi}$ and $\Phi = \widetilde{\Phi} + \Phi''$. The latter is considered to account for compressibility effects. As the growth of ice particles is a time-dependent process, the flow is assumed to be unsteady. Therefore, the unsteady Favre-averaged Navier–Stokes (FANS) equations expressing the conservation of the gas-phase global mass, momentum, and energy were solved. In Cartesian coordinates ($\boldsymbol{i}$, $\boldsymbol{j}$, $\boldsymbol{k}$), these equations read as follow with some modeling assumptions.[34]

$$\frac{\partial \overline{\rho}_g}{\partial t} + \frac{\partial}{\partial x_i}\left(\overline{\rho}_g \tilde{u}_{i,g}\right) = 0 \tag{2}$$

$$\frac{\partial}{\partial t}\left(\overline{\rho}_g \tilde{u}_{i,g}\right) + \frac{\partial}{\partial x_j}\left(\overline{\rho}_g \tilde{u}_{i,g}\tilde{u}_{j,g}\right) = \frac{\partial}{\partial x_j}\left(-\overline{P}_g \delta_{ij} + \widetilde{\tau}_{ij}^{visc} + \widetilde{\tau}_{ij}^{turb}\right) \tag{3}$$

$$\begin{aligned}\frac{\partial}{\partial t}\left(\overline{\rho}_g \tilde{e}_g^{tot}\right) + \frac{\partial}{\partial x_j}\left(\overline{\rho}_g \tilde{u}_{j,g}\tilde{e}_g^{tot} + \tilde{u}_{j,g}\overline{p}_g\right) \\ = \frac{\partial}{\partial x_j}\left(\tilde{q}_{j,g}^{visc} + \tilde{q}_{j,g}^{turb}\right) - \frac{\partial}{\partial x_j}\left(\tilde{u}_{i,g}\left(\widetilde{\tau}_{ij}^{visc} + \widetilde{\tau}_{ij}^{turb}\right)\right)\end{aligned} \tag{4}$$

Solving Eqns. (2)-(4) provides the primary variables of the mean flow $\overline{\rho}_g$, the velocity field $\tilde{\boldsymbol{u}}_g = \left(\tilde{u}_g, \tilde{v}_g, \tilde{w}_g\right)$, and the total energy $\tilde{e}_g^{tot}$, such as $c_{p,g}$ denotes the specific heat μ_g the dynamic viscosity, $\mu_{t,g}$ the eddy viscosity, Pr_g the Prandtl number, and $Pr_{t,g}$ the turbulent Reynolds number of the gas phase. The latter physical properties are all functions of $\tilde{T}_g$, which was derived from the total energy using Eq. (5). The averaging of nonlinear terms on the right-hand side of Eqns. (3) and (4) yields the Reynolds stress $\widetilde{\tau}_{ij}^{turb}$ and the turbulent heat flux $\tilde{q}_{j,g}^{turb}$, in addition to their laminar (or viscous) counterparts$\widetilde{\tau}_{ij}^{visc}$.and $\tilde{q}_{j,g}^{visc}$, given by Eqns. (6)−(9), respectively, for a Newtonian fluid.

$$\tilde{e}_g^{tot} = c_{v,g}\tilde{T}_g + \frac{\tilde{u}_{k,g}\tilde{u}_{k,g}}{2} + \frac{\widetilde{u''_{k,g}u''_{k,g}}}{2} \tag{5}$$

$$\widetilde{\tau}_{ij}^{visc} = \mu\left(\frac{\partial \tilde{u}_{i,g}}{\partial x_j} + \frac{\partial \tilde{u}_{j,g}}{\partial x_i} - \frac{2}{3}\frac{\partial \tilde{u}_{k,g}}{\partial x_k}\delta_{ij}\right) \tag{6}$$

$$\tau_{ij}^{turb} = -\overline{\rho_g u''_{i,g}\, u''_{j,g}} = \mu_{t,g}\left(\frac{\partial \tilde{u}_{i,g}}{\partial x_j} + \frac{\partial \tilde{u}_{j,g}}{\partial x_i} - \frac{2}{3}\frac{\partial \tilde{u}_{k,g}}{\partial x_k}\delta_{ij}\right) - \frac{1}{3}\overline{\rho}_g \widetilde{u''_{k,g}u''_{k,g}}\delta_{ij} \tag{7}$$

$$\tilde{q}_{j,g}^{visc} = c_{p,g}\frac{\mu_g}{Pr_g}\frac{\partial \tilde{T}_g}{\partial x_j} \tag{8}$$

$$\tilde{q}_{j,g}^{turb} = c_{p,g}\frac{\mu_{t,g}}{Pr_{t,g}}\frac{\partial \tilde{T}_g}{\partial x_j} \tag{9}$$

To compute the mixture composition in the gas phase ($\Phi_{\mathrm{g}} = \tilde{Y}_a\Phi_{\mathrm{a}} + \tilde{Y}_w\Phi_{\mathrm{w}}$), the mass fractions of air and water vapor ($\tilde{Y}_a$ and $\tilde{Y}_w$, respectively) were derived with Eqns. (10) and (11) defined as follow:

$$\frac{\partial}{\partial \mathrm{t}}\left(\bar{\rho}_g\tilde{Y}_w\right) + \frac{\partial}{\partial x_i}\left(\bar{\rho}_g\tilde{Y}_w\tilde{u}_{i,g}\right) - \frac{\partial}{\partial x_i}\left(\left(\frac{\mu_g}{\sigma_g} + \frac{\mu_{t,g}}{\sigma_{t,g}}\right)\frac{\partial \tilde{Y}_w}{\partial x_i}\right) = -\overline{\omega}_{\mathrm{ice}} \tag{10}$$

$$\widetilde{Y_a} = 1 - \tilde{Y}_w \tag{11}$$

Equation (10) translates the mass conservation of water vapor where the source term $\overline{\omega}_{\mathrm{ice}}$ on the right-hand side is the rate of condensed matter representing the mass transfer due to ice-particle growth. This coupling term is presented in greater detail in the next section. The variables σ_g and $\sigma_{t,g}$ denote the Schmidt number and the turbulent Schmidt number, respectively taken as being equal to 1[35] and 0.9[27, 28].

Lastly, the eddy viscosity $\mu_{t,g}$ term introduced by the Boussinesq approximation (Eq. (7)) was modeled using the Realizable $k-\varepsilon$ model [36] to close the set of equations. This model is known to provide improved predictions in terms of the dissipation rate for round jets.[37] It was chosen after comparing three eddy-viscosity models to the available experimental data in the case of compressible coaxial jets. Validation tests are presented below in Sec 5.1. The $k-\varepsilon$ Realizable formulation uses two transport equations: one for the turbulent kinetic energy k and one for the dissipation rate ε, such as:

$$S_{ij} = \frac{1}{2}\left(\frac{\partial \tilde{u}_{i,g}}{\partial x_j} + \frac{\partial \tilde{u}_{j,g}}{\partial x_i}\right) \tag{12}$$

$$\mu_{t,g} = \bar{\rho}_g C_\mu \frac{k^2}{\varepsilon} \tag{13}$$

$$\frac{\partial}{\partial \mathrm{t}}\left(\bar{\rho}_g k\right) + \frac{\partial}{\partial x_i}\left(\bar{\rho}_g k\tilde{u}_{i,g}\right) = -\frac{\partial}{\partial x_i}\left(\frac{\mu_{t,g}}{\sigma_k}\frac{\partial k}{\partial x_i}\right) + 2\mu_{t,g}S_{ij}\cdot S_{ij} - \bar{\rho}_g\varepsilon \tag{14}$$

$$\frac{\partial}{\partial t}\left(\bar{\rho}_g\varepsilon\right) + \frac{\partial}{\partial x_i}\left(\bar{\rho}_g\varepsilon\tilde{u}_{i,g}\right) = \frac{\partial}{\partial x_i}\left(\frac{\mu_{t,g}}{\sigma_\varepsilon}\frac{\partial \varepsilon}{\partial x_i}\right) + 2C_{1\varepsilon}\mu_{t,g}\frac{\varepsilon}{k}S_{ij}\cdot S_{ij} - C_{2\varepsilon}\bar{\rho}_g\frac{\varepsilon^2}{k+\sqrt{\nu_g\varepsilon}} \tag{15}$$

where $S_{ij} = \frac{1}{2}\left(\partial\tilde{u}_{i,g}/\partial x_j + \partial\tilde{u}_{j,g}/\partial x_i\right)$ represent the deformation rate of the mean flow. C_μ,. σ_k, σ_ε, $C_{1\varepsilon}$, and $C_{2\varepsilon}$ are the model constants (see [34, 38]).

3.3 Dispersed-phase equations and microphysics model

3.3.a Particles motion

At cruise conditions, the number density of physical particles is so high that a modeling simplification is required to save simulation time. For example, a typical value for emitted soot particles from an engine nozzle is about 10^{11} #·m^{-3}.[39] Therefore, computational particles are considered as spheres of radius r_p, with each representing N physical particles.[40] Numerically, soot and ice particles are treated as passive tracers since their size and relaxation time are relatively small compared to the characteristic scales of the gas-phase flow (for ice particles $\tau_p \sim 10^{-5}$ s with the largest r_p of a few microns).[41] Thus, they have

the same velocity as the carrier phase, but the drag and gravity forces are neglected since they have neither mass nor volume. The equation governing particle movement reads as follows:

$$\frac{d\boldsymbol{x}_p}{dt} = \tilde{\boldsymbol{u}}(\boldsymbol{x}_p, \mathrm{t}) \tag{16}$$

where $\boldsymbol{x}_p$ is the particle position vector.

3.3.b Ice-particle growth

In contrails, ice-particle growth is due to condensation of water vapor onto suitable nucleation sites on pre-activate particles (mostly soot particles).[8] The ratio between the local water vapor partial pressure (P_w) and the saturated vapor pressure with respect to liquid water $\left(P^0_{w,liq}\right)$ defines the saturation ratio[5] noted S:

$$S = \frac{P_w\left(\tilde{T}_p\right)}{P^0_{w,liq}\left(\tilde{T}_p\right)} \tag{17}$$

such as the local pressure P_w is calculated according to Dalton's law:

$$P_w\left(\tilde{T}_p\right) = \mathrm{X}_w P_{tot} \tag{18}$$

where X_w is the mole fraction of water vapor and P_{tot} is the absolute total pressure. When the saturation ratio is above 1, heterogeneous ice nucleation takes place and spherical-shaped ice particles form and grow in the dilution plume. In this study, the microphysics of ice-crystal growth was modeled, while the processes of soot activation[42] and homogeneous ice nucleation[43] were not taken into account. Therefore, the transition from continuum to molecular regime is supposed as being instantaneous.[44]

The mass change of a single-particle (computational) growth due to condensation/evaporation effects can be expressed by a diffusion law as described by the Fukuta and Walter [44] model, which describes the change of both particle mass and size as follows:

$$\dot{m}_p = \frac{dm_p}{dt} = \frac{4\pi\rho_p r_p\,(S - A)}{C_T A + C_\rho} \tag{19}$$

$$\dot{r}_p = \frac{dr_p}{dt} = \frac{S - A}{r_p(C_T A + C_\rho)} \tag{20}$$

where m_p denotes the mass of a particle p, ρ_p the particle density, and A the Kelvin effect (defined in appendix A). The factors C_T and C_ρ control the water-vapor temperature and air density just above the particle surface. The detailed formulations of both factors can be found in the appendix A. Therefore, we obtain the mass variation of each ice crystal and a fortiori the vapor mass variation. This leads to the coupling term $\overline{\omega}_{\mathrm{ice}}$ in Eq. (10), which can be derived as follows:

$$\overline{\omega}_{\mathrm{ice}} = n \sum_{p=1}^{N_{com}} \dot{m}_p \tag{21}$$

where n is the number density of particles contained in a volume cell V, such that $n = N_p/V$. The total number of computational particles is N_{com}, each of them representing N_p physical particles. More details about the model are available in Fukuta and Walter [44] The latter model was implemented in a microphysical module and coupled to the CFD commercial code in Simcenter STAR-CCM+ v13.04. A detailed description of the numerical configuration is provided below.

4. NUMERICAL METHODOLOGY

The CFD solver is based on a cell-centered finite-volume approach for unstructured grids.[20] The SIMPLE algorithm[45] was used to solve the flow governing equations. A second-order upwind scheme was used for space discretization, while time integration was achieved with a second-order Euler scheme. For the model of ice-particle growth, a fourth-order Runge-Kutta scheme was used to discretize the Equation (20) of particle size change. The discretization of the Equation (20) is presented in appendix B. The microphysical module was implemented as a user-defined function in the commercial CFD code in Simcenter STAR-CCM+ v13.04. The script of the microphysical module (coded in C) can be downloaded from.[46] The methodology for coupling with the CFD solver is detailed in Figure 3. At each time step, the primary flow variables of both gas- and dispersed-phase are derived from the CFD solver. The pressure and temperature at each grid point help to compute the thermodynamic variables (P_w, $P^0_{w,liq}$, C_T, and C_ρ), allowing derivation of the local saturation ratio. The residence time (τ_p) of each particle is computed at each time step. Radius of new particles (τ_p=0) is initialized with a monodisperse distribution using an initial radius of $r_{p,0} = 20\ nm$, as per numerical studies.[22, 27] The number density of soot particles was set to $n = 10^{11}$ #.m^{-3}, which corresponds to an emission index EI_{soot}, of 4×10^{14} particles per kg of fuel according to in situ measurements.[39] The radius of old particles ($\tau_p > 0$) was recovered from a particle-radius table. For the following time steps, the evolution of particle radius depends on the local saturation-ratio values. Nonsaturated particles keep the same radius, while saturated particles grow. The rates of change for their mass ($\dot{m}_p$) and size ($\dot{r}_p$) were computed with Eqns. (19) and (20). As such, the particle-radius table was updated and the mass-transfer term $\overline{\omega}_{ice}$ derived with Eq. (21). The coupling term was injected into the CFD solver to correct the water-mass fraction in the following time step.

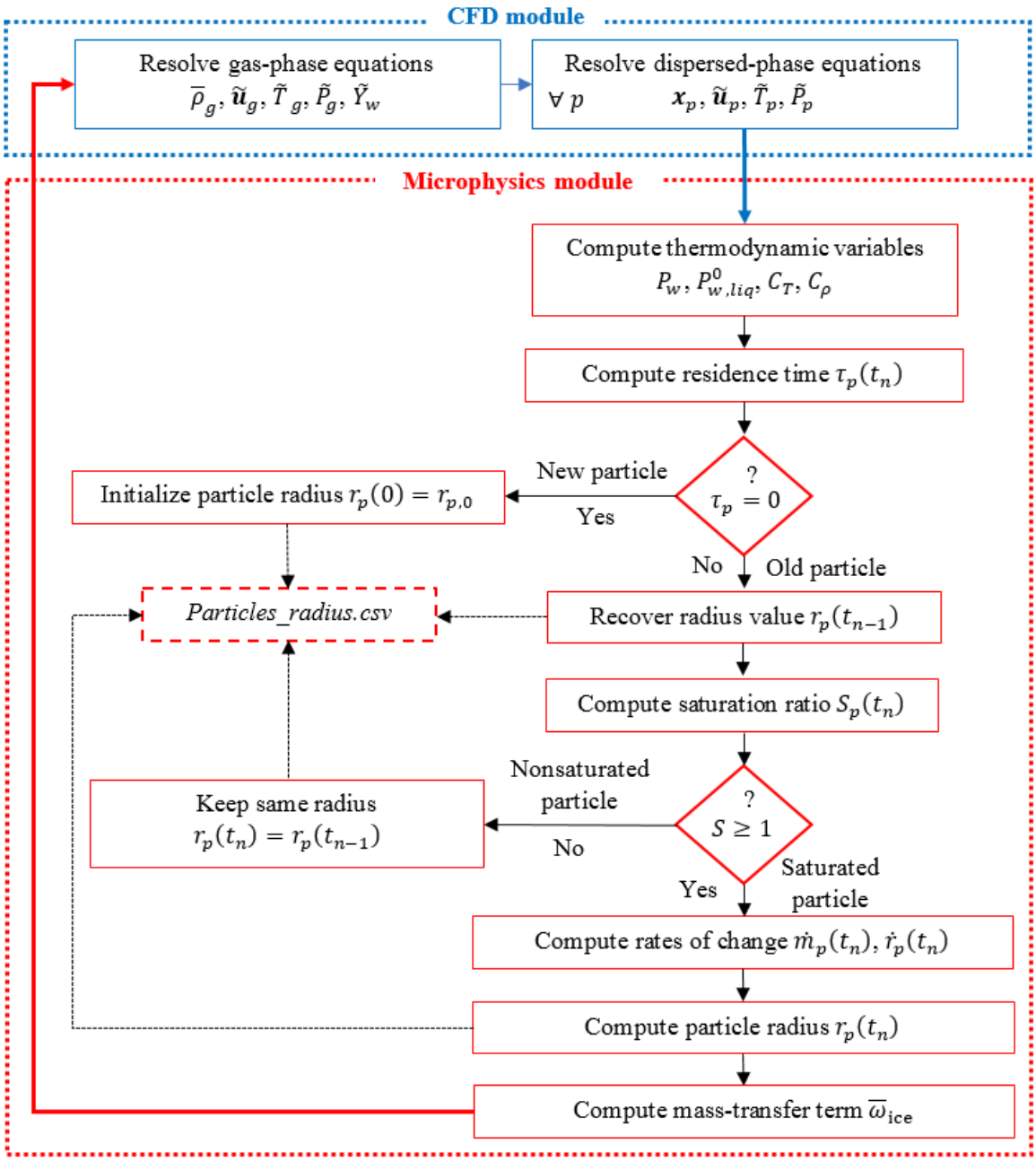

Figure 3: Schematic of the CFD-microphysics coupling for modeling ice-particle growth

5. VALIDATION TESTS AND RESULTS

Two validation tests were performed to assess the reliability of the CFD-microphysics model presented above for studying ice-particle growth in the exhaust jet of an aircraft engine. In the first test, the model's gas-phase resolution (i.e., jet dynamics and turbulence) was assessed with experimental results from the canonical case of compressible coaxial jets. This validation test made it possible to choose the most suitable turbulence model. In the second test, the model's microphysical resolution in terms of dilution and ice-particle properties (size, distribution, optical depth) were assessed in the exhaust jet of a CFM56-3 engine at realistic cruise flight conditions.

5.1 Compressible coaxial turbulent jets

5.1.a Computational domain and grid

Guitton, Tinney [47] experimentally characterized the flow dynamics and turbulence in the case of isothermal compressible coaxial jets of air. This experiment was used as a validation test case for our computational model. As shown in Figure 4, the nozzle had a length $L_{noz} = 0.158$ m and was composed of two jets: an inner primary jet, whose diameter was $D_p = 0.055$ m, and an outer secondary jet with a diameter of $D_s = 0.1$ m. The mean flow was assumed to be axisymmetric. Indeed, it has been observed experimentally that the vortex structures forming from the rollup of the shear–layers remain axisymmetric over a distance of a few diameters[48]. Hence, the computational domain was the two-dimensional rectangular box measuring $40D_s \times 15D_s$ based on the half-nozzle model, and the Reynolds-averaged Navier–Stokes (RANS) equations were solved in cylindrical coordinates $(O, \vec{r}, \vec{y})$. Two velocity-inlet boundaries were used for the engine primary- and secondary-jet flows, with corresponding values of $U_p = 170\ m.s^{-1}$ and $U_s = 120\ m.s^{-1}$, respectively (Figure 4). A symmetry condition was applied to the centerline (bottom boundary), while the remaining boundaries were treated as ambient-pressure outlet. A no-slip boundary condition was used on nozzle walls (5 mm thick).

A grid convergence study was carried out using three grids: coarse (290,110 cells), medium (618,651 cells), and fine (1,227,567 cells), respectively labeled grid 1, 2, and 3. The GCI method[49] was used to compute the discretization errors. Results of grid errors based on the axial velocity at a point probe located in the mixing layer between the two exhaust jets ($r = 0.5D_p$, $y = 10D_s$) were sufficiently low: $\mathrm{GCI}^{12}_{\mathrm{coarse}} = 1.45\%$ and $\mathrm{GCI}^{23}_{\mathrm{fine}} = 0.94\%$. As such, the medium grid was selected for computations. This mesh configuration had a total of 35 prismatic layers next to all wall boundaries, which ensured a $y^+ \leq 1$.

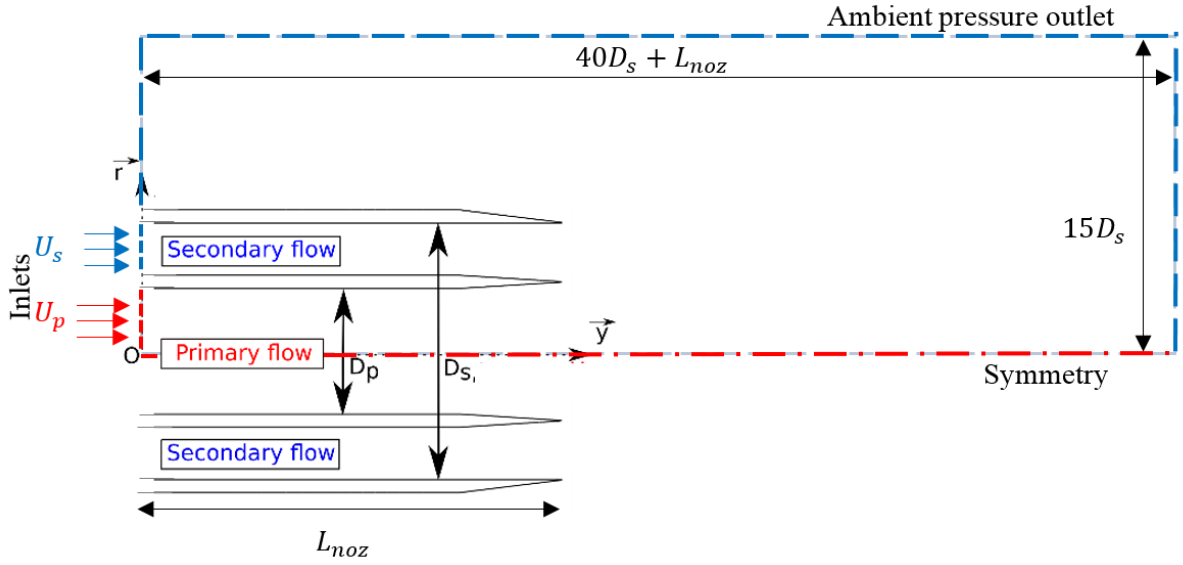

Figure 4: Scheme of the computational domain with nozzle geometry and boundary conditions

5.1.b Jet dynamics and turbulence statistics

The mixing process and associated turbulence effects have a significant impact on the dilution and ice-particle microphysics in an exhaust jet.[32] As such, the model's gas-phase resolution was first validated by studying the performance of three eddy viscosity turbulence models: $k-\varepsilon$ Standard [36], $k-\varepsilon$ Realizable [50], and $k-\omega$ SST [51]. This comparative study covered first- and second-order statistics, i.e., mean axial velocity, turbulent kinetic energy (TKE), and the Reynolds stress.

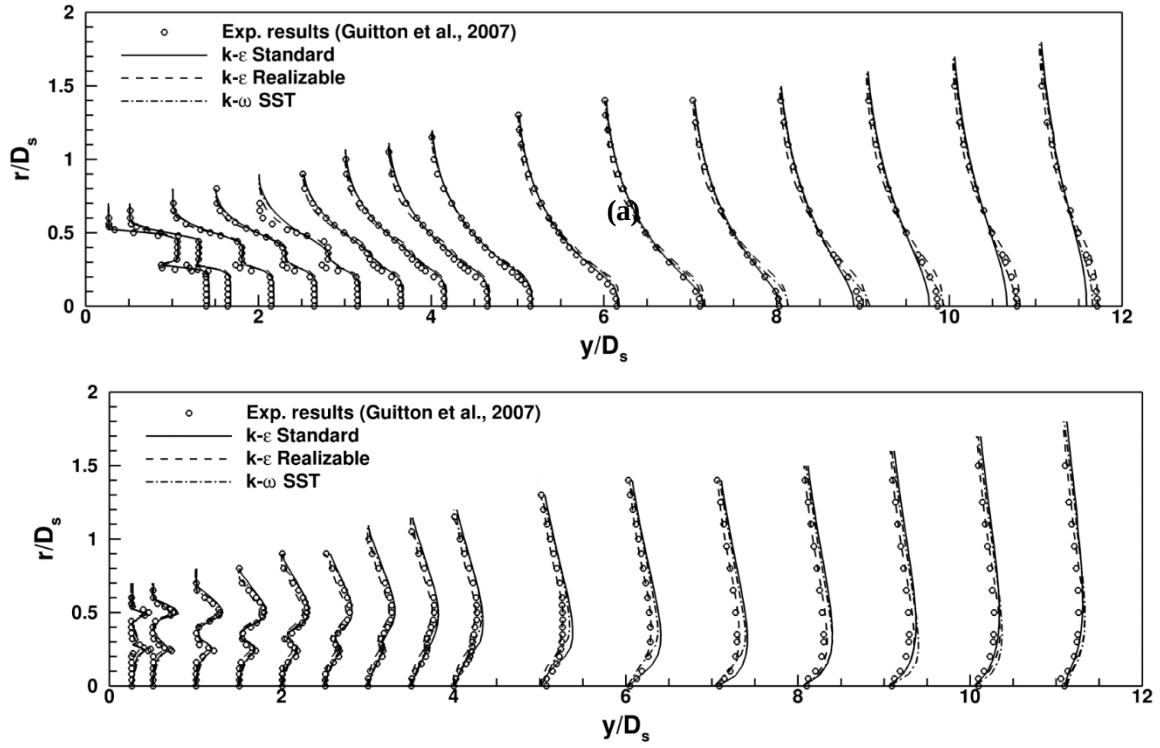

Figure 5 presents the cross-sectional profiles of the exhaust flow against experimental data.[31] Results of axial velocity profiles (

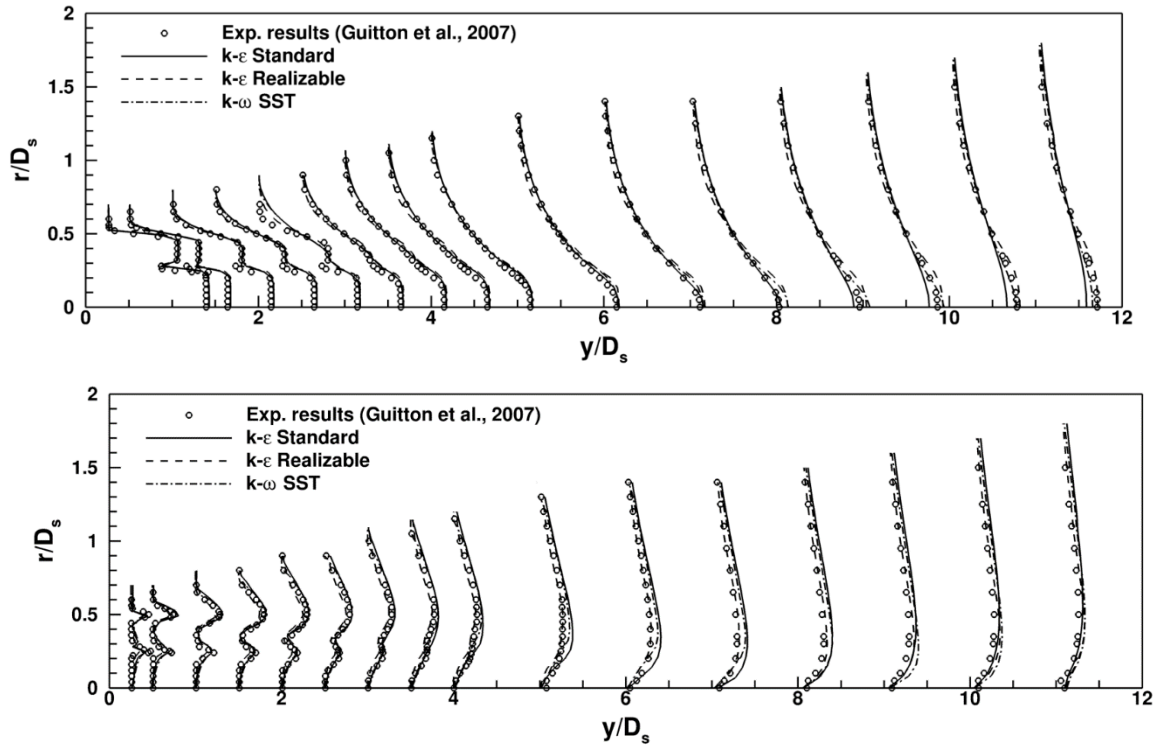

Figure 5-a) confirm that the predictions of the three tested turbulence models are satisfactory overall. The Standard and SST versions slightly overestimated the axial velocity on the external part of the jet (i.e., $r \geq 0.5D_s$). Small discrepancies can also be observed near the primary-jet centerline (i.e., $y \geq$

$7D_s$) for the $k-\varepsilon$ Standard, while the Realizable version seems to offer the best fit for experimental measurements.[32] The Reynolds-stress profiles (

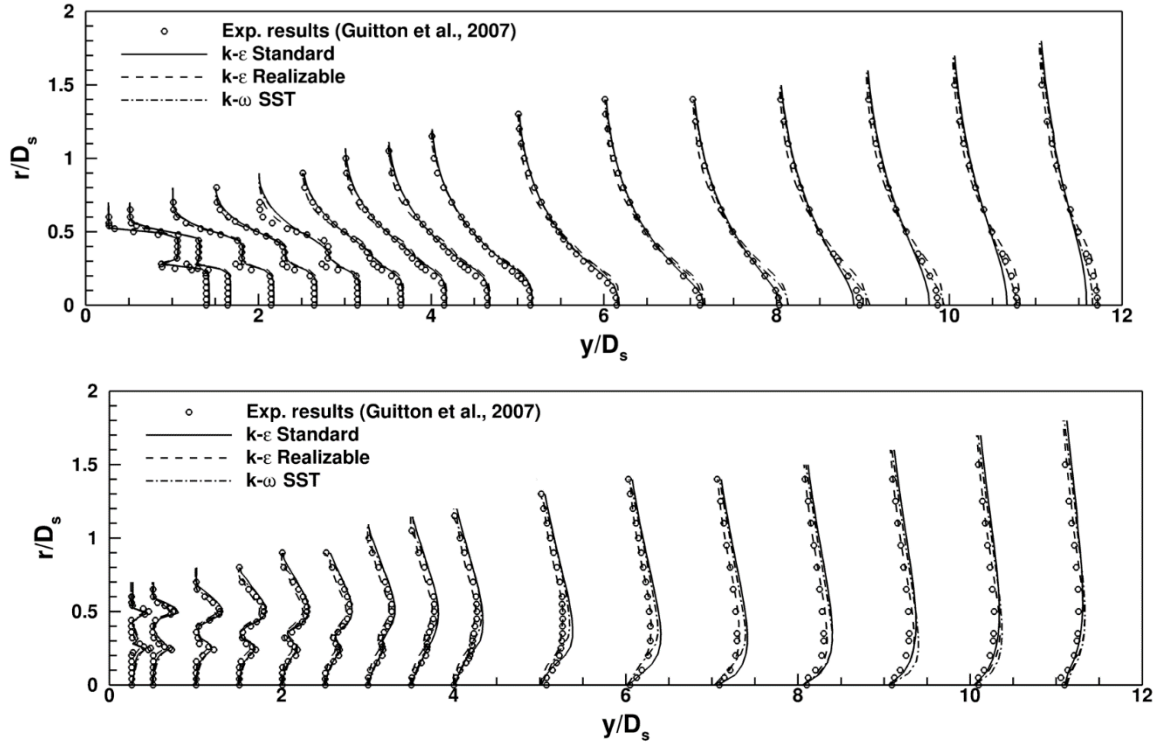

Figure 5-b) also confirm the latter conclusion in which the Standard and SST models overestimated the experimental profiles for $y \geq 5D_s$.

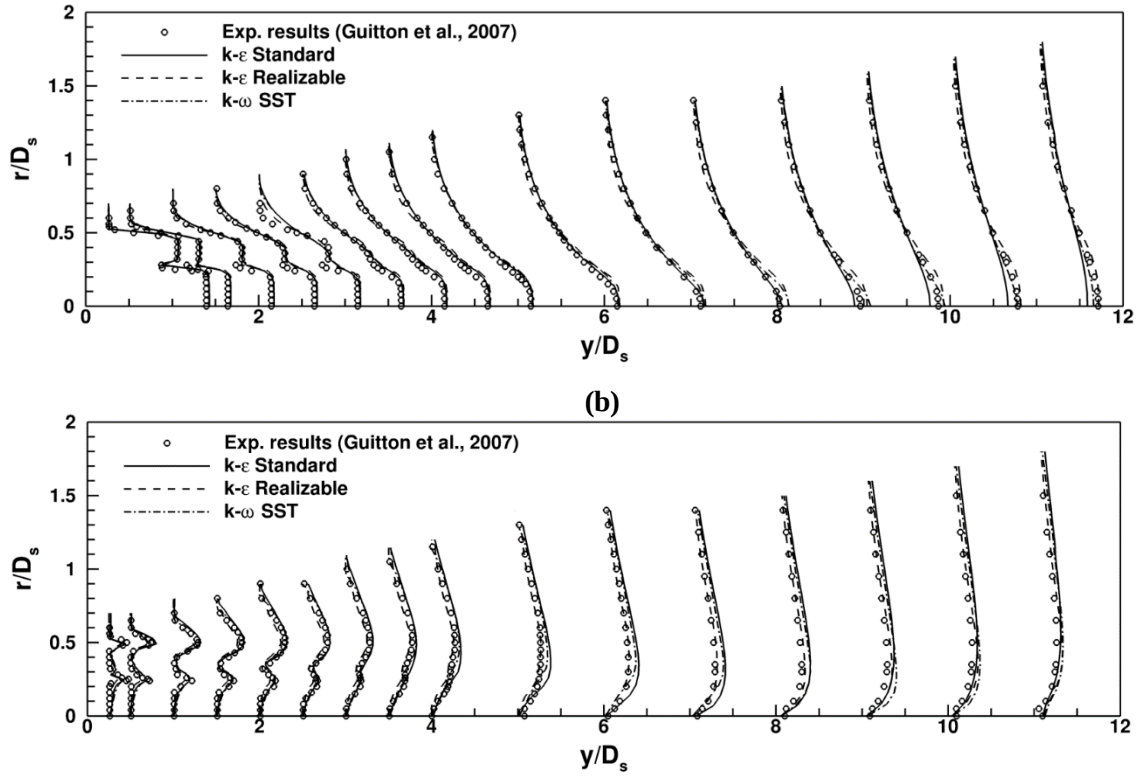

Figure 5: Comparison of exhaust-flow cross-sectional profiles for the three turbulence models tested against experimental results[31]: (a) axial velocity; (b) Reynolds stress

To better assess the discrepancies observed near the jet axis in

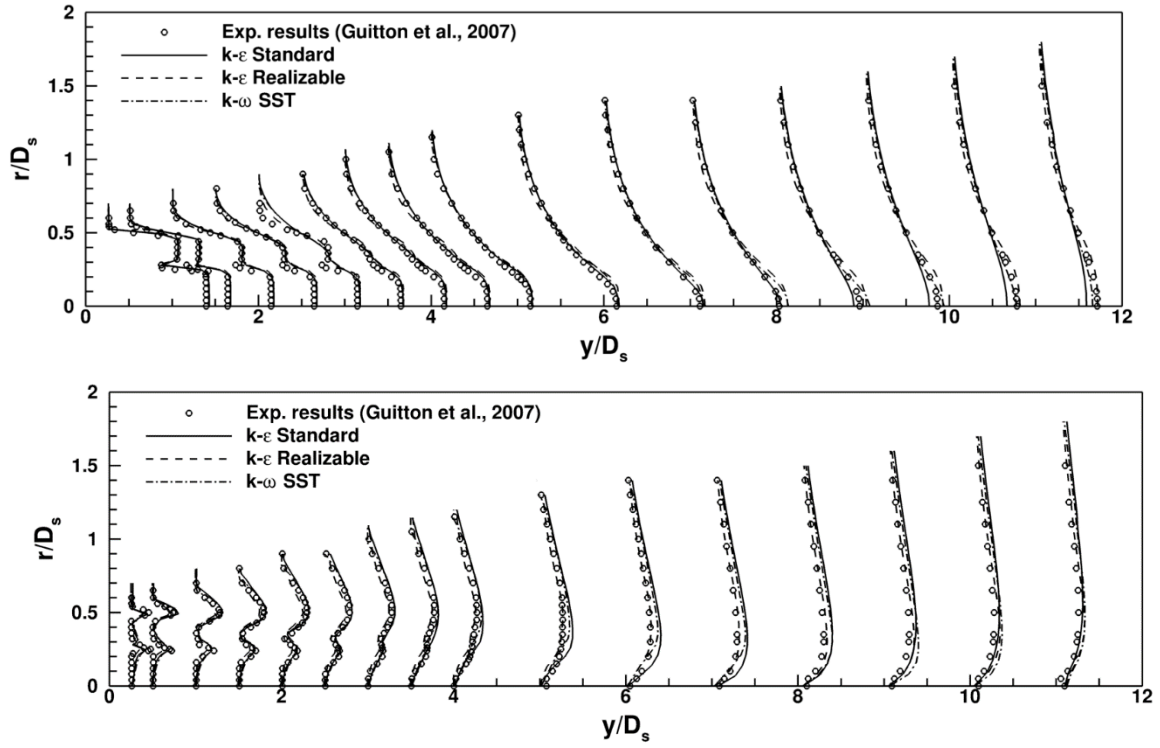

Figure 5-a, the performance study on turbulence models was carried out along the primary-jet centerline (see the results in Figure 6). The three models tested yielded similar performance in the potential core region (Figure 6-a). In contrast, both velocity decay and TKE increase (Figure 6-b) were best captured by the $k-\varepsilon$ Realizable model. Quantitatively, the $k-\varepsilon$ Realizable provided the lowest mean relative error with respect to experimental data on the mean axial velocity: 2.2% compared to 3.8% and 4.9% for $k-\omega$ SST and $k-\varepsilon$ Standard, respectively. Based on this comparative study, the $k-\varepsilon$ Realizable was selected.

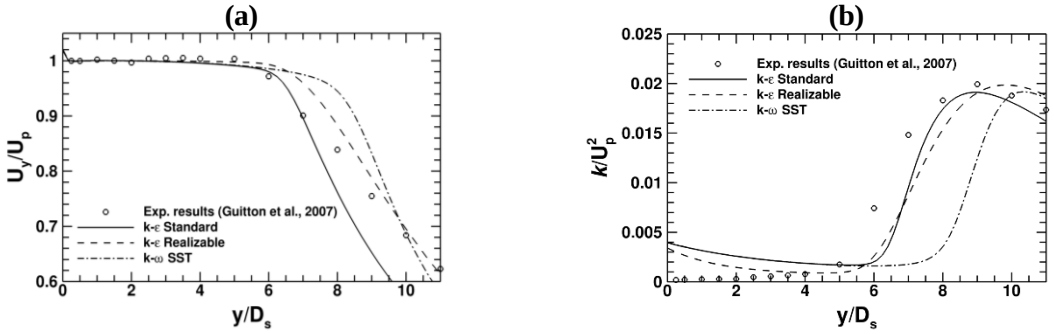

Figure 6: Comparison of primary-jet flow results for the three turbulence models tested against experimental results[31]: (a) axial velocity, (b) turbulent kinetic energy

5.2 Contrail formation in the CFM56-3 exhaust jet

5.2.a Computational domain and grid

Ice-particle formation was modeled in the exhaust plume of the CFM56-3 engine at realistic cruise flight conditions that ensure contrail formation.[27] The engine speed was set at $U_{cruise} = 252$ m.s^{-1} and ambient conditions were taken at 35,000 ft. The static temperature and pressure values were $T_{amb} = 219$ K and $P_{amb} = 23{,}800$ Pa, respectively. The mass fraction of water vapor in ambient air was set at $Y_{amb} = 6.08 \cdot 10^{-5}$ to account for 60% relative humidity for comparison with numerical results.[27]

As the mean flow was assumed to be axisymmetric, only the 90° sector based on the engine nozzle was considered for URANS calculations, as shown in Figure 7. The geometry of the CFM56-3 short-cowl nozzle is composed of a core and a bypass flow whose diameters are $D_c = 0.646$ m and $D_b = 1.586$ m. The nozzle configuration is representative of modern commercial turbofan engines,[52] in which a central plug is included to encourage early mixing between the core and bypass flows (hereafter the inner shear layer). The exhaust conditions used by Garnier, Baudoin [53] were used in this study (see Table 1). According to Paoli, Nybelen [32], physical soot particles in the range $10^6 - 10^8$ preserves the statistical reliability of the simulation results. As such, 10^7 physical particles were used herein. This ensures 40,000 computational particles, and a total number of emitted soot particles at $n = 10^{11}$ #.m^{-3}.

Table 1: Exhaust conditions of the CFM56-3 engine[53]

Core flow	Mach, $\mathbf{M_c}$	1
	Velocity, U_c (m.s^{-1})	480
	Static temperature, T_c (K)	580
	Number density of soot particles, n (#.m^{-3})	10^{11}
	Number of computational particles, N_{com} (#)	4 10^4
	Initial soot-particle diameter, $r_{p,0}$ (nm)	20
	Soot-particle distribution	Monodisperse
	Mass fraction of water vapor, Y_c	3.5 10^{-2}
Bypass flow	Mach, M_b	1
	Velocity, U_b (m.s^{-1})	311
	Static temperature, T_b (K)	242

As shown in Figure 7, the computational domain had a radius $R = 5D_b$ and a length $L = 76\ D_b$ to ensure ambient pressure at far-field boundaries. Three inlet sections were used upstream: a freestream pressure inlet (P^0_{amb}, T^0_{amb}), a bypass pressure inlet (P_b, T_b), and a core pressure inlet (P_c, T_c). A no-slip adiabatic condition was imposed on engine walls, while a symmetry condition was used on both lateral planes A turbulence intensity of 10% was used for the exhaust jets, as per Garnier et al.[53], while a value of 0.1% was applied on both freestream and far-field boundaries (P_{amb}, T_{amb}). Remaining boundaries were treated with a far-field condition.

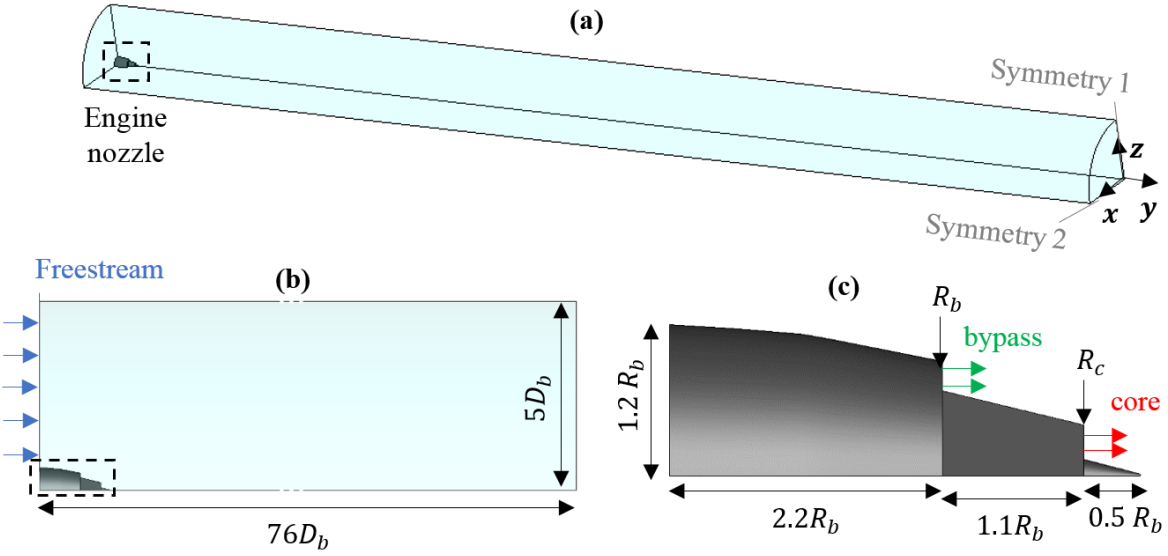

Figure 7: Computational domain and boundary conditions for the CFM56-3, short-cowl nozzle: (a) isometric view, (b) 2D view, (c) nozzle geometry

The geometry and mesh of the computational domain were generated with ANSYS ICEM CFD software.[54] A grid convergence study was performed on the gaseous phase using three grids: coarse (4.35M cells), medium (9.8M cells), and fine (20.9M cells), respectively labeled grid 1, 2, and 3. The mean errors computed in the inner shear layer (i.e., between the core and the bypass jets) for the static temperature, water-vapor mass fraction, and core axial velocity are below 1% (see Table 2). Furthermore, discretization errors estimated using the GCI method[49] at a probe point ($r = 0.7D_c$, $y = 10D_b$) were sufficiently low with the medium mesh. As such, computations were only performed on the medium grid.

The medium grid is mainly composed of hexahedral elements, as shown in Figure 8. Three cell numbers n_r, n_θ, and n_z characterize the global mesh in cylindrical coordinates (r, θ, z). Refinement blocks were used in the exhaust jet and shear layer, where gradients are expected to be relatively high. Table 3 presents the cell numbers on each boundary condition for the medium mesh. The minimum cell size in the inner shear layer was $\Delta y = 10^{-3}$ m, $\Delta x = \Delta z = 5 \cdot 10^{-5}$ m, compared to $\Delta y = 10^{-3}$ m, $\Delta z = \Delta x = 10^{-2}$ m in the outer shear layer (between the freestream and bypass flow). The near-wall refinement ensured a maximum y^+ of unity, which makes it possible to resolve the boundary layer. The mesh in the far field is relatively coarser with cells about $\Delta y = 0.2$ m, $\Delta x = \Delta z = 1.09$ m. A time step $\Delta t = 10^{-3}$ s was chosen ensuring a maximum Courant–Friedrichs–Lewy (CFL) number below 1 in the entire domain except in the potential core region where the flow speed is equal to core exit velocity $U_c = 480$ m.s^{-1} ($M_c = 1$) and the CFL reached a value of 10.

Table 2: Grid study results: mean relative error ε, standard deviation σ, and GCI index[53] between grids 1 (coarse), 2 (medium) and 3 (fine) in the inner shear layer ($r = 0.7D_c$)

Flow Variable	Static Temperature $\tilde{T}_g$	$(H_2O)_v$ Mass Fraction $\tilde{Y}_w$	Axial Velocity $\tilde{w}_g$
$\varepsilon^{12}_{\text{coarse}}$ ($\sigma^{12}_{\text{coarse}}$), %	0.2 (10^{-3})	0.6 ($3\cdot10^{-3}$)	0.4 ($1.9\cdot10^{-3}$)
$\text{GCI}^{12}_{\text{coarse}}$, %	0.13	1.47	0.69
$\varepsilon^{23}_{\text{fine}}$ ($\sigma^{23}_{\text{fine}}$), %	3.8 10^{-3} ($4.6\cdot10^{-4}$)	0.4 ($3\cdot10^{-3}$)	0.2 ($1.4\cdot10^{-3}$)
$\text{GCI}^{23}_{\text{fine}}$, %	0.03	1.01	0.22

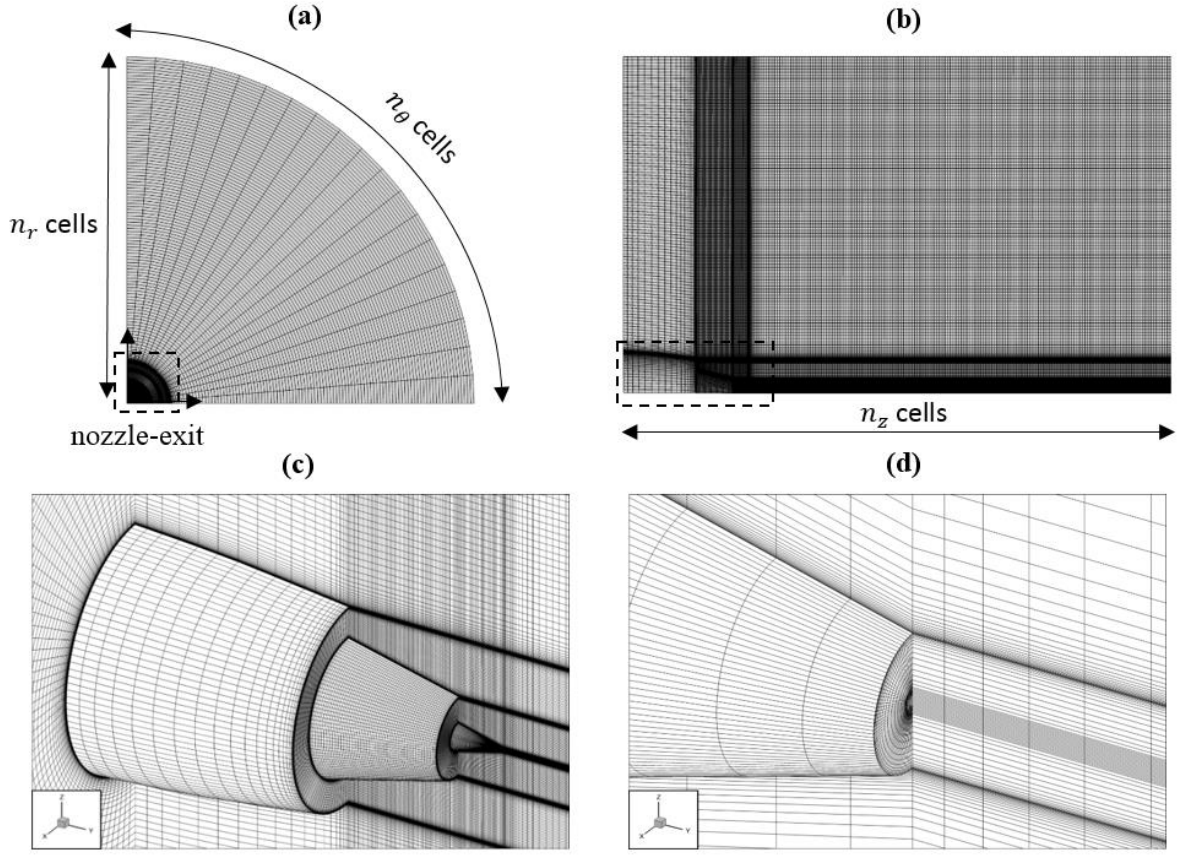

Figure 8: Computational grid for the medium mesh: (a) axial view, (b) lateral view, (c) close-up view of the nozzle exit, (d) close-up view of the central plug

Table 3: Mesh specifications on boundary conditions for the medium configuration

Boundary Conditions	Number of Cells		
	n_r	n_θ	n_z
Freestream inlet	130	20	-
Core inlet	70	20	-
Bypass inlet	60	20	-
Freestream-bypass wall	-	20	20
Bypass-core wall	-	20	50
Short-cowl wall	-	20	25
Symmetry planes	280	-	1895
Top plane	-	20	1895
Far-field outlet	280	20	-

5.2.b Jet flow and plume dilution

Figure 9-a and -b present the stream-wise contours of the axial mean velocity and Mach number, respectively, for the CFM56-3 plume. Since both dual-stream jets were at sonic conditions (M = 1), weak shock waves were observed near the exhaust sections and edges (Figure 9-b); similar behavior was reported at nozzle-exit flows.[55, 56] A flow separation on the central plug can be seen in the core flow due to the over-expansion shock. The velocity contours in Figure 9-a show that the potential core length was about $5D_b$; this distance is comparable to both experimental ($5.4D_b$)[52] and numerical ($5D_b$)[57] values.

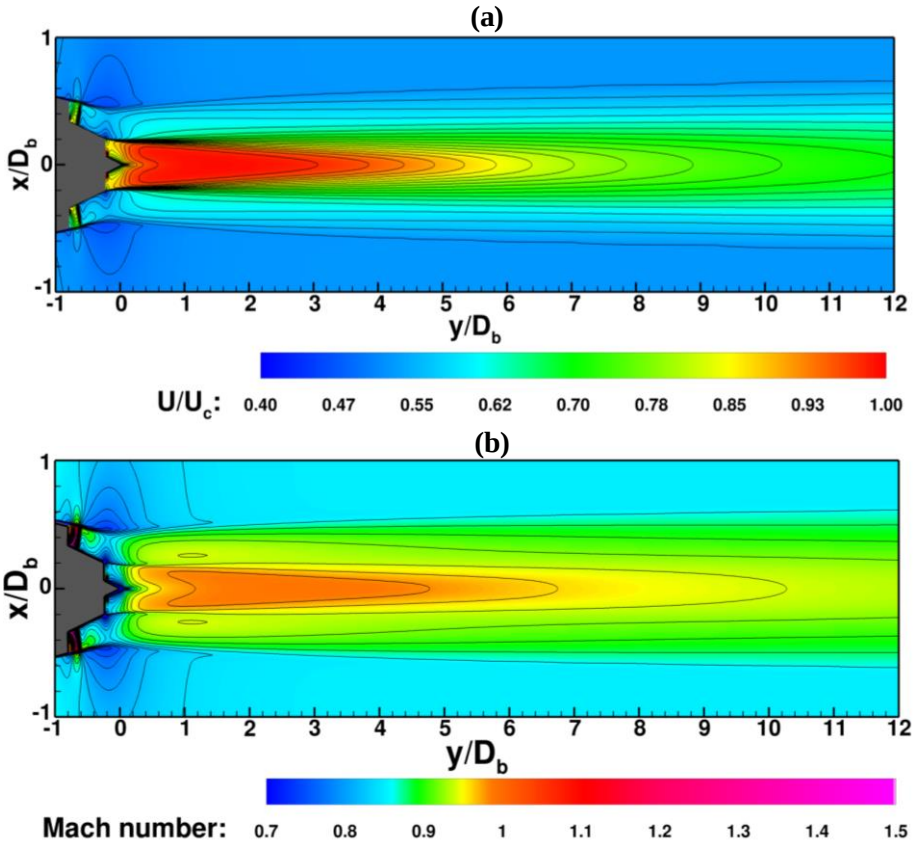

Figure 9: Stream-wise (xy-plane) contours of (a) axial mean velocity and (b) Mach number

The dilution ratio defined by Schumann, Schlager [58] was used to characterize the evolution of flow variables (such as temperature and contrail diameter) along the exhaust plume. The dilution ratio based on a passive scalar Z was calculated as

$$N_Z = \frac{N_{exit}}{\tilde{Z}} \tag{22}$$

where N_{exit} is the dilution factor at the exhaust section [58] and $\tilde{Z}$ is the ratio of the amount of fluid from the jet region to that from the freestream.[53] The latter was calculated from

$$\tilde{Z} = \frac{\tilde{Z}_{y,plume} - \tilde{Z}_{i,atm}}{\tilde{Z}_{i,jet} - \tilde{Z}_{i,atm}} \tag{23}$$

where $\tilde{Z}_{y,plume}$ is the passive scalar concentration in the exhaust plume, $\tilde{Z}_{i,atm}$ is the initial atmospheric concentration, and $\tilde{Z}_{i,jet}$ denotes the initial jet concentration. The concentration measurement was taken along the plume centerline.

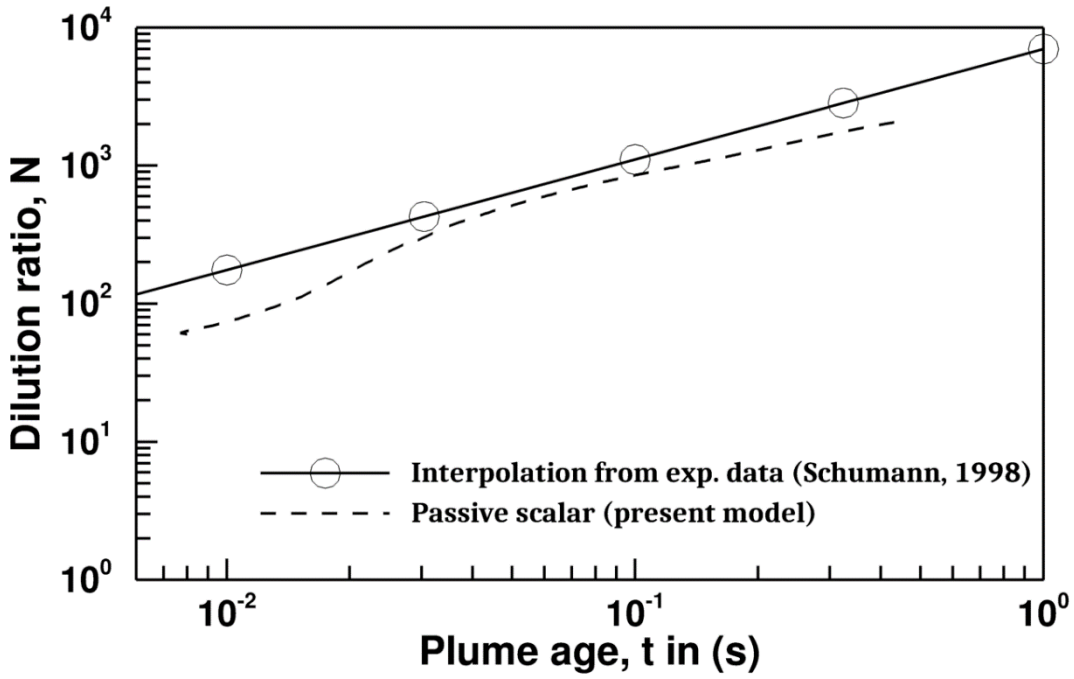

Figure 10: Evolution of the predicted dilution ratio along the primary jet centerline against in-flight measurements[58]

Figure 10 shows the evolution of the dilution ratio N_Z as function of the plume age compared to the bulk mean dilution interpolated from in-flight measurements.[59] For instance, the interpolation was based on a large set of data from more than 70 plume encounters with the DLR Falcon research aircraft and the NASA ER-2 aircraft.[59] It should be noted that the bulk dilution ratio corresponded to the radial average of the local dilutions ratios within the plume at a given distance from the nozzle exit. This explains why the predicted dilution ratio along the core jet as seen in figure (Figure 10) was relatively smaller than the bulk interpolation of the mixed primary and secondary jets (as also highlighted by Schumann, Ström [59]), especially near the engine exhaust. Even with that, the variations of the dilution ratio in the simulated plume are of the same order of magnitude as the bulk mean interpolation. The study of ice-crystal properties during contrail formation is presented in the next section.

5.2.c *Contrail formation and ice-particle properties*

Figure 11-a presents the spatial distribution of ice-particle radii in the plume exhaust. Up to a distance of $10D_b$ downstream, the jet temperature was high enough to prevent ice coating of soot particles with an initial radius of $r_{p,0} = 20\ nm$. The mixing with ambient air downstream cooled the plume, and the first ice crystals can be observed within a thin layer of the plume edge at $y = 10D_b$. More ice particles formed and grew subsequent to the thickening of the external shear layer by transverse diffusion up to $y \sim 50D_b$ where water-vapor condensation reached the plume core.

The rate of condensation along the exhaust plume was fully determined by the local ice saturation ratio S, which, in turn, depends on the local temperature $\tilde{T}_g$ and water mass fraction $\tilde{Y}_w$ [32]. Figure 11–b and –c compare two transverse cross-sectional distributions at $y = 30D_b$ and $72D_b$ from the core exhaust section, respectively. Both engine core and bypass sections are represented by black circles (solid line). At $y = 30D_b$, the particles were spatially distributed over a circular area of diameter $2D_b$. Ice condensation was only observed on the external shear layer ($r \geq 0.5D_b$) while soot particles transported along the plume core remain under-saturated. The transverse dispersion of ice crystals enhanced by mixing with ambient air downstream resulted in a radial expansion of the plume up to a diameter $3D_b$ at $y = 72D_b$. At this section, the center of the plume was fully saturated and, due to the relatively high water content in the core jet, ice particles seemed to grow faster along the plume core ($r \leq D_b$), up to a radius about 50 $r_{p,0}$, as compared to the plume edge. At the outer edge of the plume; ice particle radii reached a constant value around 500 nm for y/D_b > 50. Indeed, the growth of ice-particles (i.e. condensation rate) is mainly governed by the local value of the saturation ratio S, which is below 1 in the outer edge of the plume. As a consequence, the ice-particles do not grow in the outer edge and reach a constant size of 500 nm.

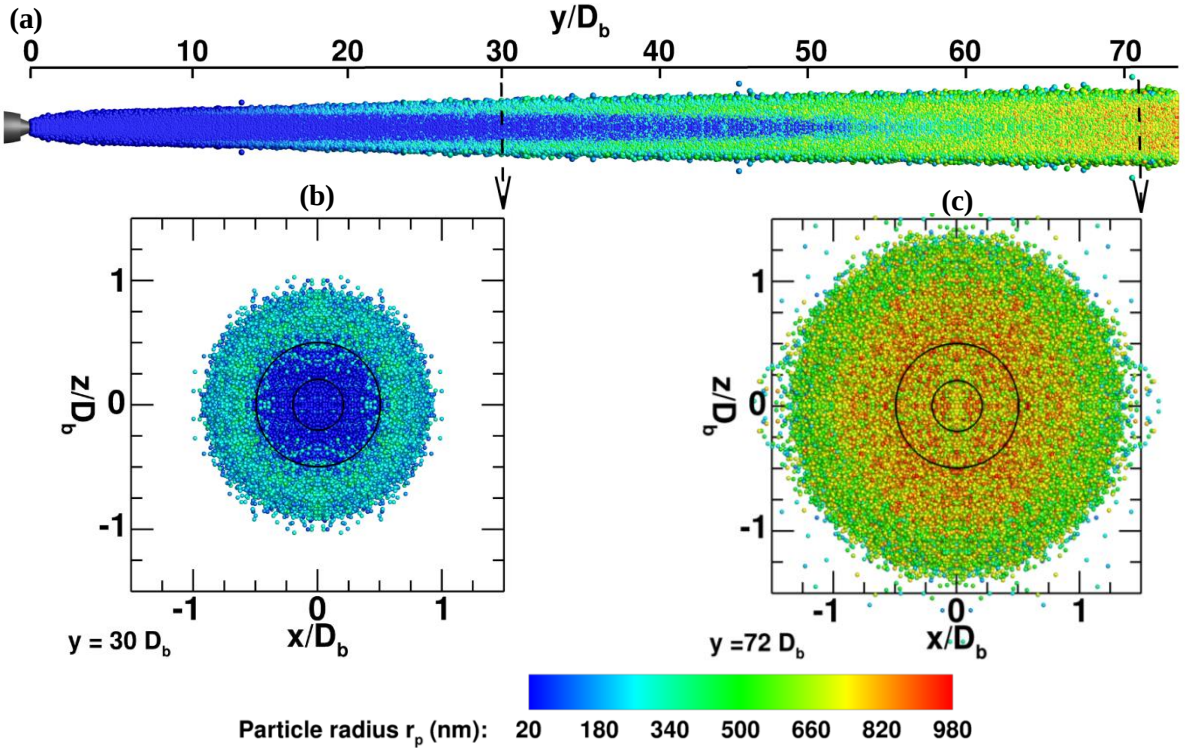

Figure 11: Spatial distribution of particle radii: (a) longitudinal cross-sectional distribution, transverse cross-sectional distributions at (b) $y = 30D_b$ and (c) $y = 72D_b$

The evolution of the saturation ratio along the exhaust jet shows that the plume was fully saturated, i.e., $S = 1$, at a distance about $55D_b$ behind the nozzle exit (see Figure 12). This is consistent with the numerical results of Khou [60] obtained behind a full aircraft geometry with an Eulerian approach for particle tracking. Since the growth rate of ice crystals is directly related to the local saturation-ratio value, the mean particle radius follows the same trend as the bulk mean saturation ratio. It should be noted that that the mean particle radius $< r_p(y) >$ corresponds to the arithmetic average of particle radii over the subdomain of length h centered on the position y, defined as[32]

$$< r_p(y) >= \frac{1}{h} \int_{y-h/2}^{y+h/2} r_p \, dy' = \frac{1}{N} \sum_{i=1}^{N} r_{p,i} \tag{24}$$

where N is the particle number within the considered subdomain and $r_{p,i}$ is the radius of a given particle i. Overall, the results show that our model captures well the global dynamic of ice-particle growth compared to the numerical prediction by Khou [60]. The mean radius was initially constant near the engine exhaust and started growing around $y = 10D_b$. At 0.5 s of the plume age ($y = 72D_b$), the mean particle radius was in the good range of 500 to 1000 nm, as confirmed by several numerical studies.[15, 16, 61]

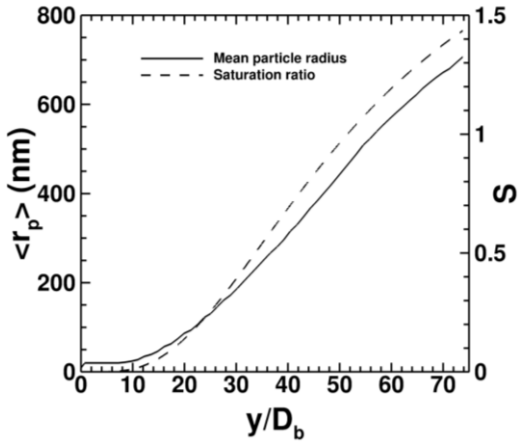

Figure 12: Evolutions of the mean particle radius and the saturation ratio along the jet plume

To better assess the particle-size distribution along the exhaust plume, the probability density functions (PDF) were investigated at four distances: $20D_b$, $30D_b$, $50D_b$, and $72D_b$ behind the engine exhaust (see Figure 13). Results show that the PDF distributions shifted towards large radii following the growth of ice crystals along the exhaust plume. Moreover, Gaussian distributions were obtained from $y = 50D_b$ indicating polydispersed distributions of ice-particle radii, as observed in other numerical studies.[22, 32]

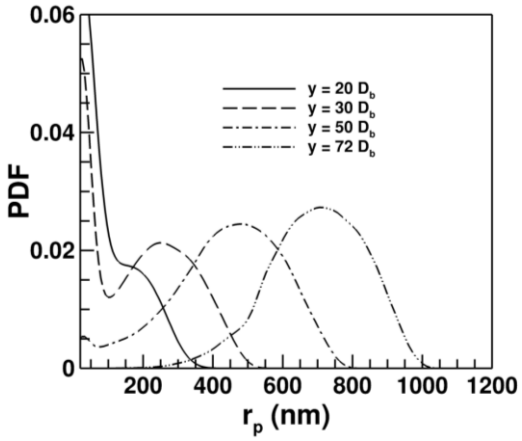

Figure 13: Probability density functions (PDF) of particle radius at four axial distances: $20D_b$, $30D_b$, $50D_b$, and $72D_b$

Lastly, the visibility in the predicted contrail was assessed with the optical depth τ. This parameter measures the attenuation of radiation passing through clouds and is often reported at a wavelength in the visible part of the radiation spectrum.[7] The optical depth τ was evaluated as formulated by Naiman, Lele [62]

$$\tau = \sum_{i=1}^{N_{com,g}} \pi r_p^2 Q_{ext} \frac{N_g}{\Delta V} \tag{25}$$

where $N_{com,g}$ denotes the number of computational particles in the grid cell, N_g the total number of physical particles in the grid cell, and ΔV its volume. Equation (26) approximates the Mie extinction efficiency Q_{ext} at a given wavelength λ_w, such as the refractive index for ice of $\mu_r = 1.31$ and the wavelength of visible light is considered as $\lambda_w = 0.55$ µm.

$$Q_{ext} = 2 - \frac{4}{e}\left[\sin(e) - \frac{1-\cos(e)}{e}\right] \tag{26}$$

$$e = \frac{4\pi r_p(\mu_r - 1)}{\lambda_w} \tag{27}$$

The visibility threshold of jet contrails is defined by the criterion $\tau \geq 0.5$.[61] Figure 14 shows that the predicted contrail from the CFM56-3 engine was visible at a distance about 26 m from the engine exhaust. The latter value is good agreement with the in situ observations reporting visible contrails at a distance in the range 10 to 30 m.[59, 63]

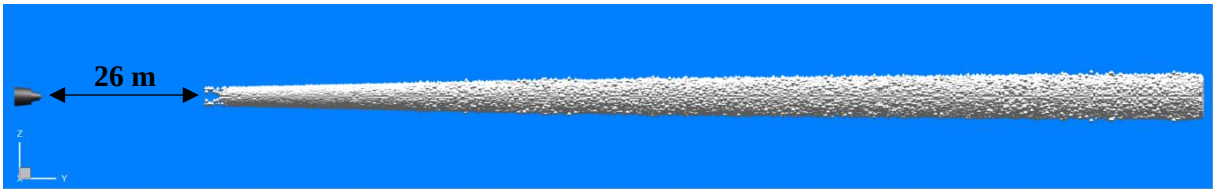

Figure 14: Visible contrail predicted in the near-field of the CFM56-3 engine using the visibility criterion $\tau \geq 0.5$

The comprehensive analysis performed shows that this model's predictions are consistent with available numerical data. Such model can be used in future investigations to characterize the impact of complex

nozzle geometries—such as chevron nozzles—on the optical and microphysical properties of near-field contrails. Research perspectives to be explored next involve the interactions of soot and sulfur species in the early plume. This requires the implementation of a gas-phase chemistry with the microphysics of volatile particles.

6. CONCLUSION

This paper demonstrated the feasibility of Eulerian–Lagrangian CFD coupling with ice microphysics to predict the near-field contrails starting from the nozzle-exit geometry of the CFM56-3 engine. The microphysical module implemented accounts for the main process of ice-particle growth based on heterogeneous nucleation. Two validation tests were performed to assess the reliability of the proposed CFD-microphysics model. In the first validation, the canonical case of compressible coaxial jets made it possible to choose the Realizable $k-\varepsilon$ turbulence model based on its good performance in terms of the jet dynamics and turbulence properties. In the second test case, the model's microphysical resolution was assessed in the exhaust jet from the CFM56-3 engine at realistic cruise flight conditions. The predicted plume dilution showed good agreement with available experimental data. Qualitatively, the spatial distribution of ice particles revealed that the first ice crystals were formed at the plume edge at a distance of about $10D_b$ from the engine exhaust. Further downstream, ice particles formed and grew subsequent to the thickening of the external shear layer due to transverse diffusion. Results of the saturation ratio show that the plume core axis was saturated at a distance of about $55D_b$. Polydispersed distributions of particle radii were obtained in the simulated contrail with the largest ice particle reaching a radius about 1 μm in the plume core. As the jet evolved downstream, the particle-size distributions shifted toward larger particles. Lastly, the optical-depth analysis shows that the predicted contrail was visible around 26 m behind the engine exhaust, which is consistent with contrail observations.

The model presented herein is intended to serve as the foundation for more advanced numerical simulations to investigate the impact of complex nozzle-exit geometries, such as chevron nozzles. The implementation of gas-phase chemistry and volatile-particle microphysics are planned to extend the model capabilities.

Acknowledgments

The authors thank Charles E. Tinney for providing data measurements on coaxial jets conducted at the Laboratoire d'Etudes Aérodynamiques (LEA) in Poitiers, France. Computations were made on the Beluga supercomputer at the École de technologie supérieure (ÉTS) in Montréal, managed by Calcul Quebec and Compute Canada. The operation of this supercomputer is funded by the Canada Foundation for Innovation (CFI), the Ministère de l'Économie, de la science et de l'innovation du Québec (MESI), 531, and the Fonds de recherche du Québec-Nature et technologies (FRQ-NT). The authors would also like to acknowledge the financial support of Safran Aircraft Engine for this work. This work is part of the Safran Industrial Research Chair on the Development of Sustainable Aero-Propulsion Systems at ÉTS.

Declaration of conflicting interests

The Authors declare that there is no conflict of interest.

ORCID iD

Sébastien Cantin https://orcid.org/0000-0002-9502-3162

Appendix A: Equations for the Microphysical Module

This appendix begins with a description of the factors C_T and C_ρ in the microphysical model.[44] This is followed by a description of the thermodynamics equations to calculate the saturation pressure, density, surface tension, and latent heat of water.

The factor C_T was calculated as:

$$C_T = \frac{L_w^2 M_w \rho_p}{k_g R \tilde{T}_p^2 \mathrm{f}_{3\alpha}} \tag{28}$$

where L_w is the heat latent of water vapor (J.kg^{-1}), M_w is the molar fraction of water (M$_w$ = 18.015 10^{-3} kg.mol$^{-1)}$, ρ_p is the particle density of water vapor (kg.m^{-3}), k_g is the conductivity of the gas (W.m^{-1}.K^{-1}), R is the universal gas constant (R = 8.314 J.mol^{-1}.K^{-1}), $\tilde{T}_p$ the particle temperature (K), and $\mathrm{f}_{3\alpha}$ a correction factor for the temperature difference between the particle's boundary layer and ambient air.

The conductivity of the gas was calculated from[64]:

$$k_g = \left(5.69\ 10^{-5} + \left(\tilde{T}_g - 273.15\right)0{,}017\ 10^{-5}\right) 4.18\ 10^{2} \tag{29}$$

The factor $\mathrm{f}_{3\alpha}$ was calculated from:

$$\mathrm{f}_{3\alpha} = \frac{r_p}{r_p + \dfrac{k_g \sqrt{2\pi M_a R \tilde{T}_p}}{\alpha p_\infty \left(C_{p,a} - R/2\right)}} \tag{30}$$

where M_a is the molar fraction of air (M$_a$ = 28.964 10^{-3} kg.mol^{-1}), α is the accommodation coefficient with a consensus value of 0.68[65], p_∞ is the atmospheric pressure (Pa), and $C_{p,a}$ is the molar heat of air at constant volume (J.K^{-1}.mol^{-1}).

The factor C_ρ was calculated as:

$$C_\rho = \frac{R \tilde{T}_p \rho_p}{P_w^0 D_w M_w \mathrm{f}_{3\beta}} \tag{31}$$

where P_w^0 is the saturation pressure (Pa), D_w is the diffusivity of water vapor (m^2.s^{-1}), and $\mathrm{f}_{3\beta}$ is a correction factor for the vapor-density difference between the particle's boundary layer and the ambient air.

The factor A in Eqs. (19) and (20) was calculated as:

$$A = \exp\left(\frac{2\sigma_p M_w}{r_p \rho_p r_g \tilde{T}_g}\right) \tag{32}$$

where σ_p denotes the surface tension of water.

The diffusivity of water vapor was calculated from[64]:

$$D_w = \left(0.211\left(\frac{\tilde{T}_g}{273.15}\right)^{1,94}\frac{1.013\ 10^5}{p_g}\right)10^{-4} \quad (33)$$

The factor $f_{3\beta}$ was derived from:

$$f_{3\beta} = \frac{r_p}{r_p + \frac{D_w}{\beta}\sqrt{\frac{2\pi M_w}{RT_p}}} \quad (34)$$

where β is the condensation coefficient taken as 0.022.[65]

The thermodynamic equation of the model is described. These equations depend on the particle temperature. The model considered the state of water. When the water was liquid ($\tilde{T}_g$ (x_p) ≥ +5°C), Eqns. (35) to (38) were used. When the water was ice ($\tilde{T}_g$ (x_p) < +5°C), Eqns. (39) to (42) were used.

The density of liquid water (kg.m^{-3}) was calculated from[64]:

$$\rho_{liq}(\tilde{T}_g) = \left(0.9998 + 0.86\ 10^{-4}\left(\tilde{T}_g - 273.15\right) - 0.108\ 10^{-4}\left(\tilde{T}_g - 273.15\right)^2\right)10^3 \quad (35)$$

The surface tension of liquid water (J.m^{-2}) was calculated from[66]:

$$\sigma_{liq}(\tilde{T}_g) = \left(76.1 - 0{,}155\left(\tilde{T}_g - 273.15\right)\right)10^{-3} \quad (36)$$

The condensation latent heat of liquid water (J.kg^{-1}) was calculated from[64]:

$$L_{liq}\left(\tilde{T}_g\right) = \left(597.3\left(\frac{273.15}{\tilde{T}_g}\right)^{0.167+3.61\ 10^{-4}\tilde{T}_g}4.18\ 10^3\right) \quad (37)$$

The saturation pressure of liquid water (Pa) was calculated from[67]:

$$P^0_{w,liq}(\tilde{T}_p) = 100\ 10\text{^}\left(10.79574\left(1 - \frac{273.16}{\tilde{T}_p}\right) - 5.028\ log_{10}\left(\frac{\tilde{T}_p}{273.16}\right) + 1.50475\ 10^{-4}\left(1 - 10^{\left(-8.2969\left(\frac{\tilde{T}_p}{273.16}-1\right)\right)}\right) + 0.42873\ 10^{-3}\left(10^{\left(-4.76955\left(1-\frac{\tilde{T}_p}{273.16}\right)\right)} - 1\right) + 0.78614\right) \quad (38)$$

The density of ice was (kg.m^{-3}) calculated from[64]:

$$\rho_{ice}\left(\tilde{T}_g\right) = \left(0.91676 - 1.75\ 10^{-4}\left(\tilde{T}_g - 273.15\right) - 5\ 10^{-7}\left(\tilde{T}_g - 273.15\right)^2\right)10^3 \quad (39)$$

The surface tension of ice (J.m^{-2}) was calculated from[66]:

$$\sigma_{ice}(\tilde{T}_g) = \left(104.6 - 0.095\left(\tilde{T}_g - 273.15\right)\right)10^{-3} \quad (40)$$

The sublimation latent heat of liquid water (J.kg^{-1}) was calculated from[64]:

$$L_{ice}(\tilde{T}_g) = \left(\left(597.3\left(\frac{273.15}{\tilde{T}_g}\right)^{0.167+3.61\,10^{-4}\,\tilde{T}_g}\right) + \left(79.7 + 0.485\left(\tilde{T}_g - 273.15\right) - 2.5\,10^{-3}\left(\tilde{T}_g - 273.15\right)^2\right)\right) 4.18\,10^3 \quad (41)$$

The saturation pressure of ice (Pa) was calculated from:

$$P^0_{w,ice}(\tilde{T}_p) = 100\ 10^{\left(\frac{9.5(\tilde{T}_p-273.15)}{(\tilde{T}_p-273.15)+265.5}+0.7858\right)} \quad (42)$$

Appendix B: Discretization of the ice particle growth equation

This appendix describe the discretization of ice particle growth Eq. (20) with a fourth order Runge-Kutta method. The four constants k_1, k_2, k_3, k_4 of the Runge-Kutta method are presented below:

$$\begin{cases} k_1 = \dfrac{\Delta t}{r_p(t_{n-1})}\left[\dfrac{S - exp\left(\dfrac{A'}{r_p(t_{n-1})}\right)}{C_T\, exp\left(\dfrac{A'}{r_p(t_{n-1})}\right) + C_\rho}\right] \\ k_2 = \dfrac{\Delta t}{\left[r_p(t_{n-1}) + \dfrac{k_1}{2}\right]}\left[\dfrac{S - exp\left(\dfrac{A'}{r_p(t_{n-1}) + \dfrac{k_1}{2}}\right)}{C_T\, exp\left(\dfrac{A'}{r_p(t_{n-1}) + \dfrac{k_1}{2}}\right) + C_\rho}\right] \\ k_3 = \dfrac{\Delta t}{\left[r_p(t_{n-1}) + \dfrac{k_2}{2}\right]}\left[\dfrac{S - exp\left(\dfrac{A'}{r_p(t_{n-1}) + \dfrac{k_2}{2}}\right)}{C_T\, exp\left(\dfrac{A'}{r_p(t_{n-1}) + \dfrac{k_2}{2}}\right) + C_\rho}\right] \\ k_4 = \dfrac{\Delta t}{\left[r_p(t_{n-1}) + k_3\right]}\left[\dfrac{S - exp\left(\dfrac{A'}{r_p(t_{n-1}) + k_3}\right)}{C_T\, exp\left(\dfrac{A'}{r_p(t_{n-1}) + k_3}\right) + C_\rho}\right] \end{cases} \quad (43)$$

The factor A' is computed as follows:

$$A' = \frac{2\sigma M_w}{\rho r_g \tilde{T}_g} \quad (44)$$

where σ denotes the surface tension of water and ρ the particle density.

The new particle radius $r_p(t_n)$ is computed as follows:

$$r_p(t_n) = r_p(t_{n-1}) + (k_1 + 2k_2 + 2k_3 + k_4)/6 \quad (45)$$

Then, the condensed matter of ice particles associated to Eq. (19) is calculated as follows

$$m_p(t_n) = \frac{\rho_{ice} 4\pi}{\Delta t}\left(r_p(t_n) - r_p(t_{n-1})\right)\left(r_p(t_n)\right)^2 n \tag{46}$$

where n is the number density of particles contained in a volume cell V, such that $n = N_p/V$.

References

1. Lee DS, Fahey DW, Forster PM, et al. Aviation and global climate change in the 21st century. *Atmospheric Environment* 2009; 43: 3520-3537. DOI: http://doi.org/10.1016/j.atmosenv.2009.04.024.
2. Schumann U and Heymsfield A. On the Life Cycle of Individual Contrails and Contrail Cirrus. *Meteorological Monographs* 2017; 58: 3.1-3.24. DOI: 10.1175/amsmonographs-d-16-0005.1.
3. Nguyen TH, Nguyen-Tri P, Vancassel X, et al. Aero-thermodynamic and chemical process interactions in an axial high-pressure turbine of aircraft engines. *International Journal of Engine Research* 2019; 20: 653-669. DOI: 10.1177/1468087418772228.
4. Lewellen DC, Meza O and Huebsch WW. Persistent contrails and contrail cirrus. Part I: Large-eddy simulations from inception to demise. *Journal of the Atmospheric Sciences* 2014; 71: 4399-4419. DOI: 10.1175/JAS-D-13-0316.1.
5. Jensen EJ, Toon OB, Kinne S, et al. Environmental conditions required for contrail formation and persistence. *Journal of Geophysical Research* 1998; 103: 3929-3936. DOI: 10.1029/97JD02808.
6. Solomon S. IPCC (2007): Climate change the physical science basis. *AGUFM* 2007; 2007: U43D-01.
7. Kärcher B. Formation and radiative forcing of contrail cirrus. *Nature communications* 2018; 9: 1824.
8. Schumann U. *On Conditions for Contrail Formation from Aircraft Exhausts*. 1996, p.4-23.
9. Schumann U. A contrail cirrus prediction model. *Geoscientific Model Development* 2012; 5: 543-580. DOI: 10.5194/gmd-5-543-2012.
10. Schumann U, Mayer B, Graf K, et al. A parametric radiative forcing model for contrail cirrus. *Journal of Applied Meteorology and Climatology* 2012; 51: 1391-1406. DOI: 10.1175/JAMC-D-11-0242.1.
11. Kärcher B. Physicochemistry of aircraft-generated liquid aerosols, soot, and ice particles: 1. Model description. *Journal of Geophysical Research: Atmospheres* 1998; 103: 17111-17128. DOI: 10.1029/98JD01044.
12. Wong HW and Miake-Lye RC. Parametric studies of contrail ice particle formation in jet regime using microphysical parcel modeling. *Atmospheric Chemistry and Physics* 2010.
13. Gierens K. On the transition between heterogeneous and homogeneous freezing. *Atmospheric Chemistry and Physics* 2003; 3: 437-446. DOI: 10.5194/acp-3-437-2003.
14. Rojo C, Vancassel X, Mirabel P, et al. Impact of alternative jet fuels on aircraft induced aerosols. *Fuel* 2014.
15. Paoli R, Vancassel X, Garnier F, et al. Large-eddy simulation of a turbulent jet and a vortex sheet interaction: Particle formation and evolution in the near field of an aircraft wake. *Meteorologische Zeitschrift* 2008.
16. Vancassel X, Mirabel P and Garnier F. Numerical simulation of aerosols in an aircraft wake using a 3D LES solver and a detailed microphysical model. *International Journal of Sustainable Aviation* 2014; 1: 139-159. DOI: 10.1504/ijsa.2014.065480.
17. Unterstrasser S. Properties of young contrails – a parametrisation based on large-eddy simulations. *Atmospheric Chemistry and Physics* 2016; 16: 2059-2082. DOI: 10.5194/acp-16-2059-2016.
18. Burkhardt U and Karcher B. Process-based simulation of contrail cirrus in a global climate model. *Journal of Geophysical Research - Part D - Atmospheres* 2009; 114: D16201 (16213 pp.). DOI: 10.1029/2008JD011491.
19. Jacobson MZ, Wilkerson JT, Naiman AD, et al. The effects of aircraft on climate and pollution. Part I: Numerical methods for treating the subgrid evolution of discrete size- and composition-resolved contrails from all commercial flights worldwide. *Journal of Computational Physics* 2011; 230: 5115-5132. DOI: https://doi.org/10.1016/j.jcp.2011.03.031.
20. Lewellen DC. A Large-Eddy Simulation Study of Contrail Ice Number Formation. *Journal of the Atmospheric Sciences* 2020; 77: 2585-2604. DOI: 10.1175/jas-d-19-0322.1.
21. Unterstrasser S, Paoli R, Sölch I, et al. Dimension of aircraft exhaust plumes at cruise conditions: effect of wake vortices. *Atmospheric Chemistry and Physics* 2014: 21.
22. Garnier F, Maglaras E, Morency F, et al. Effect of Compressibility on Contrail Ice Particle Growth in an Engine Jet. *International Journal of Turbo & Jet-Engines* 2014; 31: 131. DOI: 10.1515/tjj-2013-0039.
23. Cantin S, Morency F and Garnier F. Modeling capabilities on the formation of contrails in a commercial CFD code. In: *ISABE 2019* (ed Engines ISfAB), Canberra, Autralia, September, 22-27 2019, p.14.
24. Zhang Z and Chen Q. Comparison of the Eulerian and Lagrangian methods for predicting particle transport in enclosed spaces. *Atmospheric Environment* 2007; 41: 5236-5248. DOI: https://doi.org/10.1016/j.atmosenv.2006.05.086.
25. Lewellen DC and Lewellen WS. Effects of aircraft wake dynamics on measured and simulated NOx and HOx wake chemistry. *Journal of Geophysical Research* 2001; 106: 27661-27672. DOI: 10.1029/2001JD000531.
26. Paugam R, Paoli R and Cariolle D. Influence of vortex dynamics and atmospheric turbulence on the early evolution of a contrail. *Atmospheric Chemistry and Physics* 2010; 10: 3933-3952. DOI: 10.5194/acp-10-3933-2010.
27. Khou JC, Ghedhaifi W, Vancassel X, et al. Spatial Simulation of Contrail Formation in Near-Field of Commercial Aircraft. *Journal of Aircraft* 2015.

28. Khou JC, Ghedhaifi W, Vancassel X, et al. CFD simulation of contrail formation in the near field of a commercial aircraft: effect of fuel sulfur content. *Meteorologische Zeitschrift* 2016. DOI: 10.1127/metz/2016/0761.
29. Unterstrasser S and Sölch I. Optimisation of the simulation particle number in a Lagrangian ice microphysical model. *Geoscientific Model Development* 2014; 7: 695-709. DOI: 10.5194/gmd-7-695-2014.
30. Unterstrasser S and Sölch I. Study of contrail microphysics in the vortex phase with a Lagrangian particle tracking model. *Atmospheric Chemistry and Physics* 2010; 10: 10003-10015.
31. Khain AP, Beheng KD, Heymsfield A, et al. Representation of microphysical processes in cloud-resolving models: Spectral (bin) microphysics versus bulk parameterization. *Reviews of Geophysics* 2015; 53: 247-322. DOI: 10.1002/2014rg000468.
32. Paoli R, Nybelen L, Picot J, et al. Effects of jet/vortex interaction on contrail formation in supersaturated conditions. *Physics of Fluids* 2013; 25: 053305. DOI: 10.1063/1.4807063.
33. Unterstrasser S and Görsch N. Aircraft-type dependency of contrail evolution. *Journal of Geophysical Research: Atmospheres* 2014; 119: 14,015-014,027. DOI: 10.1002/2014JD022642.
34. CD-Adapco. STAR-CCM+ Documentation Version 13.06.012. 2018.
35. Kärcher B. Transport of exhaust products in the near trail of a jet engine under atmospheric conditions. *Journal of Geophysical Research: Atmospheres* 1994; 99: 14509-14517. DOI: 10.1029/94JD00940.
36. Jones WP and Launder BE. The prediction of laminarization with a two-equation model of turbulence. *International Journal of Heat and Mass Transfer* 1972; 15: 301-314. DOI: https://doi.org/10.1016/0017-9310(72)90076-2.
37. Shaheed R, Mohammadian A and Kheirkhah Gildeh H. A comparison of standard k–ε and realizable k–ε turbulence models in curved and confluent channels. *Environmental Fluid Mechanics* 2019; 19: 543-568. DOI: 10.1007/s10652-018-9637-1.
38. Thies AT and Tam CKW. Computation of turbulent axisymmetric and nonaxisymmetric jet flows using the K-epsilon model. *AIAA Journal* 1996; 34: 309-316. DOI: 10.2514/3.13065.
39. Schröder F, Brock CA, Baumann R, et al. In situ studies on volatile jet exhaust particle emissions: Impact of fuel sulfur content and environmental conditions on nuclei mode aerosols. *Journal of Geophysical Research: Atmospheres* 2000; 105: 19941-19954. DOI: 10.1029/2000JD900112.
40. Schröder F, Karcher B, Duroure C, et al. On the transition of contrails into cirrus clouds. *Journal of the Atmospheric Sciences* 2000; 57: 464-480. DOI: 10.1175/1520-0469(2000)057<0464:OTTOCI>2.0.CO;2.
41. Paoli R, Hélie J and Poinsot T. Contrail formation in aircraft wakes. *Journal of Fluid Mechanics* 2004; 502: 361-373. 03/01. DOI: 10.1017/S0022112003007808.
42. Koehler KA, DeMott PJ, Kreidenweis SM, et al. Cloud condensation nuclei and ice nucleation activity of hydrophobic and hydrophilic soot particles. *Physical Chemistry Chemical Physics* 2009; 11: 7906-7920. 10.1039/B905334B. DOI: 10.1039/B905334B.
43. Hartmann S, Niedermeier D, Voigtlaender J, et al. Homogeneous and heterogeneous ice nucleation at LACIS: Operating principle and theoretical studies. *Atmospheric Chemistry and Physics* 2011; 11. DOI: 10.5194/acp-11-1753-2011.
44. Fukuta N and Walter LA. Kinetics of Hydrometeor Growth from a Vapor-Spherical Model. *Journal of the Atmospheric Sciences* 1970; 27: 1160-1172. DOI: 10.1175/1520-0469(1970)027<1160:kohgfa>2.0.co;2.
45. Patankar SV and Spalding DB. A calculation procedure for heat, mass and momentum transfer in three-dimensional parabolic flows. *International Journal of Heat and Mass Transfer* 1972; 15: 1787-1806. DOI: https://doi.org/10.1016/0017-9310(72)90054-3.
46. Cantin S. Emissions and Microphysical Modelling for Aircraft Plume (EMMAP), https://github.com/SebastienCantin/EMMAP (2020, accessed 4 February 2021).
47. Guitton A, Tinney CE, Jordan P, et al. Measurements in a Co-Axial Subsonic Jet. *45th AIAA Aerospace Sciences Meeting and Exhibit*. American Institute of Aeronautics and Astronautics, 2007.
48. Salvetti MV and Lombardi G. Three-Dimensional Effects on Mixing in a Coaxia Jet Configuration. In: Frisch U (ed) *Advances in Turbulence VII: Proceedings of the Seventh European Turbulence Conference, held in Saint-Jean Cap Ferrat, France, 30 June – 3 July 1998 / Actes de la Septième Conférence Européenne de Turbulence, tenue à Saint-Jean Cap Ferrat, France, 30 Juin – 3 Juillet 1998*. Dordrecht: Springer Netherlands, 1998, pp.167-170.
49. Celik IB, Ghia U, Roache PJ, et al. Procedure for Estimation and Reporting of Uncertainty Due to Discretization in CFD Applications. *Journal of Fluids Engineering* 2008; 130: 078001-078001-078004. DOI: 10.1115/1.2960953.
50. Shih T-H, Liou WW, Shabbir A, et al. A new k-ϵ eddy viscosity model for high reynolds number turbulent flows. *Computers & Fluids* 1995; 24: 227-238. DOI: https://doi.org/10.1016/0045-7930(94)00032-T.
51. Menter FR. Two-equation eddy-viscosity turbulence models for engineering applications. *AIAA Journal* 1994; 32: 1598-1605. DOI: 10.2514/3.12149.

52. Timmerman BH, Skeen AJ, Bryanston-Cross PJ, et al. Large-scale time-resolved digital particle image velocimetry (TR-DPIV) for measurement of high subsonic hot coaxial jet exhaust of a gas turbine engine. *Measurement Science and Technology* 2009; 20: 074002.
53. Garnier F, Baudoin C, Woods P, et al. Engine emission alteration in the near field of an aircraft. *Atmospheric Environment* 1997; 31: 1767-1781. DOI: https://doi.org/10.1016/S1352-2310(96)00329-9.
54. AnsysInc. *ANSYS ICEM CFD User Manual*. 2019.
55. Nair PP, Suryan A and Kim HD. Computational study on flow through truncated conical plug nozzle with base bleed. *Propulsion and Power Research* 2019; 8: 108-120. DOI: https://doi.org/10.1016/j.jppr.2019.02.001.
56. Goulos I, Stankowski T, MacManus D, et al. Civil turbofan engine exhaust aerodynamics: Impact of bypass nozzle after-body design. *Aerospace Science and Technology* 2017; 73: 85-95. DOI: https://doi.org/10.1016/j.ast.2017.09.002.
57. Xiong J, Nielsen P, Liu F, et al. Computation of High-Speed Coaxial Jets with Fan Flow Deflection. *AIAA Journal* 2010; 48: 2249-2262. DOI: 10.2514/1.J050331.
58. Schumann U, Schlager H, Arnold F, et al. Dilution of aircraft exhaust plumes at cruise altitudes. *Atmospheric Environment* 1998; 32: 3097-3103. DOI: http://dx.doi.org/10.1016/S1352-2310(97)00455-X.
59. Schumann U, Ström J, Busen R, et al. In situ observations of particles in jet aircraft exhausts and contrails for different sulfur-containing fuels. *Journal of Geophysical Research: Atmospheres* 1996; 101: 6853-6869. DOI: 10.1029/95JD03405.
60. Khou JC. *Modélisation des traînées de condensation par interaction entre l'aérodynamique, la cinétique chimique et la microphysique*. Ph.D. Dissertation, Université Pierre et Marie Curie, ONERA/EMI, Palaiseau, 2016.
61. Kärcher B, Mayer B, Gierens K, et al. Aerodynamic Contrails: Microphysics and Optical Properties. *Journal of the Atmospheric Sciences* 2009; 66: 227-243. DOI: 10.1175/2008jas2768.1.
62. Naiman AD, Lele SK and Jacobson MZ. Large eddy simulations of contrail development: Sensitivity to initial and ambient conditions over first twenty minutes. *Journal of Geophysical Research: Atmospheres* 2011; 116. DOI: 10.1029/2011JD015806.
63. Busen R and Schumann U. Visible contrail formation from fuels with different sulfur contents. *Geophysical Research Letters* 1995; 22: 1357-1360. DOI: 10.1029/95GL01312.
64. Pruppacher HR, Klett JD and Wang PK. *Microphysics of Clouds and Precipitation*. 1998, p.381.
65. Fukuta N and Myers MN. Simultaneous measurement of condensation and thermal accommodation coefficients for cloud droplet growth in due consideration of a new moving surface-boundary effect. *Journal of the Atmospheric Sciences* 2007; 64: 955-968. DOI: 10.1175/JAS3834.1.
66. Taleb D-E. *Etude microphysique et modelisation des sillages d'avions subsoniques et supersoniques*. Ph.D. Dissertation, Louis Pasteur University, Strasbourg, France, 1997.
67. Goff JA. Saturation pressure of water on the new Kelvin temperature scale. *Transactions of the American Society of Heating and Ventilating Engineers* 1957; 63: 347-354.